Synthesis and Investigation of Structural, Microstructural and Optical Properties of Iron-doped Sno2 Nanoparticles : Application in Photocatalysis

Sabrina Roguai (rog.sabrina@yahoo.fr)
Université Abbes Laghrour https://orcid.org/0000-0002-0767-0846
Abdelkader Djelloul
Université Abbes Laghrour

Research Article

Keywords: Sn1-xFexO2 nanoparticles, structural, microstructural and optical properties, photocatalysis

Posted Date: May 17th, 2021

DOI: https://doi.org/10.21203/rs.3.rs-513448/v1

Synthesis and investigation of structural, microstructural and optical properties of iron-doped SnO_2 nanoparticles : Application in photocatalysis

[1,*]Sabrina. Roguai, [2]Abdelkader. Djelloul

[1,2] LASPI[2]A Laboratoire des Structures, Propriétés et Interactions Inter Atomiques, Université Abbes Laghrour, Khenchela 40000, Algérie

Science of matter, Abbes Laghrour University, Khenchela, Algeria

*rog.sabrina@yahoo.fr

Abstract

Iron-doped tin dioxide nanoparticles $Sn_{1-x}Fe_xO_2$ ($0\% \leq x \leq 10\%$), were prepared by coprecipitation method. X-ray diffraction (XRD) patterns indicate that $Sn_{1-x}Fe_xO_2$ nanoparticles (NPs) crystallize in the tetragonal rutile-like structure. Scanning Electron Microscope (SEM) observations did not show more modification of the SnO_2 morphology with Fe addition. All the results are consistent with the fact that Fe is strongly soluble in SnO_2 host. The optical band gap energy decreased from 3.65 to 3.30 eV with increasing the iron doping concentration in the solution. Finally, the photocatalytic efficiency of $Fe_{0.05}Sn_{0.95}O_2$ nanoparticles (NPs) was examined for the degradation of MB in aqueous solution under UV irradiation. It was found that smaller bandgap of Fe doped SnO_2 photocatalyst resulted in a prominent increase in photocatalytic activity of nanoparticles against Methylene Blue (MB) under UV irradiaion.

Key words: $Sn_{1-x}Fe_xO_2$ nanoparticles, structural, microstructural and optical properties, photocatalysis.

1 Introduction

The development of nanoscale particles is a promising research theme, supported by different branches of the industry ranging from biomedical to cosmetic through catalysis. Indeed, such a particle size gives the material unique and new physical and chemical properties, not encountered with larger materials. [1-3]

Metallic oxides and in particular tin oxides are excellent examples for accessing new or improved properties. Tin oxide nanoparticles offer attractive magnetic, electrical and optical properties [4] as well as high chemical reactivity [5-7], giving them a wide range of fields of application such as biomedical, treatment of water, catalysis, gas sensors, lithium-ion accumulators [8, 9].

Tin oxide is a transparent conductive oxide of type n with a energy band gap of 3.6 eV, The structure of tin dioxide called cassiterite crystallizes in the tetragonal rutile type system represented with the parameters: a = b = 4.737 **Å** and c = 3.186 **Å** [10]. The elementary cell contains six atoms, four oxygen atoms and two tin atoms. Its space group is P4 / mnm [11]. Each tin ion Sn^{4+} is at the center of an octahedron formed by six oxygen ions O^{2-}, as long as each oxygen ion O^{2-} is at the center of an isosceles triangle formed by three ions of tinSn4 +. cation Sn^{4+} and the anion O^{2-} have the value 0.071 and 0.14 nm [12]. The oxygen vacancies formed by the transfer of an oxygen atom from a site to a normal site in the gaseous state, make it possible to obtain a semiconductor of this type. Indeed, the oxygen gap thus created has two electrons, it is then said to be neutral which can be yielded under the effect of temperature. There is then simple or double ionization thereof. The released electrons can attach to Sn^{4+} tin atoms. They then become Sn^{2+} and behave like electron donors [13,14]. It is arguably the most widely used compared to other oxides in the area of air pollution monitoring and the detection of toxic gases. [15] In fact, it has electrical properties linked to the remarkable surface adsorption. Tin oxide is also known for its catalytic properties, in particular it facilitates the decomposition of many hydrocarbons.

The doping of SnO_2 by suitable elements such as Mn, Fe, Co, Al, Mg ... etc, can improve its optical, electrical and magnetic characteristics and accelerate the race for its practical applications[16].

The addition of transition metals in the photocatalyst influences the trapping of electrons, slows down the speed of recombination of electron / hole pairs, increases the efficiency of charge transfer. It also influences the optical gap of the photocalyser by creating the energy levels inside the forbidden band which helps us to extend the spectrum of adsorption towards visible light and to take advantage of solar radiation.

Recently Fe-doped SnO_2 has attracted attention as a candidate for diluted magnetic semiconductors (DMS) [17,18]. It has the advantage of a lower surface potential barrier than

metals and a high catalytic activity, which can be very vital in the field of electron emission [19].

Many methods of synthesis of SnO_2nanopowders such as hydrothermal [20], chemical vapor deposition (CVD) [21], sol-gel [22], chemical coprecipitation [23] and spray pyrolysis have been developed [24].

In this paper, Fe doped SnO_2 nanoparticles are synthesized by coprecipitation method for photocatalytic application in the treatment of water purification. The objective that we set ourselves in this work is to study the influence of doping on the structural, microstructural, and morphological properties of the of synthesized nanostructures and their photo-catalytic performance was investigated with the degradation of Methylene Blue (MB) dye

2 Experimental Procedure

2.1 Synthesis of SnO_2 and Fe doped SnO_2 nanoparticles

The iron-doped tin oxide nanoparticles, $Sn_{1-x}Fe_xO_2$ (x= 0.00, 0.02, 0.05and 0.10), were prepared by chemical co-precipitation method[25]. For the synthesis of $Sn_{1-X}Fe_XO_2$ nanoparticles, tin chloride pentahydrate ($SnCl_4.5H_2O$), ferric chloride dihydrate (Fe $Cl_2.2H_2O$) and sodium hydroxide (NaOH) were used as precursors without further purification. All the chemicals used in the present preparation are highly pure (more than 99%) and AR grade purchased from Merck.

Initially, 0.1M $SnCl_4.5H_2O$ was dissolved in 100 ml double distilled water and maintained under agitation for 10 min. 0.3M NaOH solution was prepared separately by dissolving appropriate amount of NaOH in 50 ml double distilled water. The prepared

NaOH solution was added drop wise into the initial aqueous solution under constant stirring up to 2hrs at room temperature to reach the pH value of 12. The formed gelatinous white precipitates were filtered and then washed seven times using double distilled water and ethanol to eliminate the impurities and chlorine ions from precipitates. Dry for overnight at room temperature and dried in oven at 100 ºC for six hours. The dried white precipitates then annealed at 600 ºC for two hours followed by grinding to get fine particles. The same procedure is repeated for the remaining samples synthesized with nominal compositions of $Sn_{1-x}Fe_xO_2$ (x= 0.00, 0.02, 0.05and 0.10). These were used for various characterization techniques [26-28]

2.2 Characterization Techniques

The crystal structure of Fe-doped SnO_2 nanoparticles was determined by X-ray diffractometer (MiniFlex600) with Cu–Kα radiation, 0.15418 nm). The surface morphology of the prepared nanoparticles was studied using a scanning electron microscopy (TESCAN_VEGA3) equipped with energy dispersive X-ray spectroscopy (EDS) for chemical analysis. The infrared absorption (FTIR) spectra were recorded to examine the structure by using Thermo-Nicolet equipment in the 4000–400 cm^{-1} region. The absorbance property was studied using Parkin Elmer UV–VIS–NIR Lambda 19 spectrophotometer in the 190–1800 nm spectral range.

2.3 Photocatalytic experiments

The photocatalytic activity of $Sn_{1-x}Fe_xO2$ [x= 0.00,0.02,0.05 and 0.10] nanocomposites was evaluated by measuring the decolourization of MB under visible light irradiation at ambient temperature using a 100 W incandescent lamp as a light source. The solutions were pretreated by magnetic stirring in the dark for 30 min to achieve adsorption–desorption equilibrium of MB on the catalyst surface. Then, the solutions were irradiated each 30 min, the concentration of MB was determined by recording the variations of the absorption band maximum (**664**nm) of MB using Parkin Elmer UV–VIS–NIR Lambda 19 spectrophotometer

3 Results and discussion

3.1 X-ray diffraction – structural analysis

The XRD pattern of $Sn_{1-x}Fe_XO_2$ [x = 0, 2, 5 and 10 atm.%] nanoparticles are shown in Fig. 1. In the scan range from 10° to 90°, both the samples show the four major peaks (100), (101) , (200) and (211), which correspond well with that of cassiterite phase (JCPDS file number 01-071-0652). No secondary peak characteristic of ferric oxide phase appear for all Fe-doped samples was observed within the detection limit of used XRD, indicating that Fe ions successfully occupy lattice sites rather than interstitial sites of SnO_2 which possess a high solubility [29], and the good atomic-level blending of all constituent elements through the co-precipitation method. This important solubility of iron in SnO2 has also been recorded for many other trivalent ions, such as Ga and In [30,31].

However, the addition of Fe influences the SnO_2, XRD pattern either in intensity or in broadening of peaks, suggesting that the crystallinity and the particle size are modified by iron doping.

In $Sn_{0.98}Fe_{0.02}O_2$ sample, the maximum intensity peak characterizing the structure rutile corresponding to (110) , (101), (200) and (211)plane which decreasing with doping level. The reduced diffraction intensity with doping may be due to impurities that oppose the growth of SnO_2. It is also due to the movement of Sn^{4+} ions in the interstitial sites

and also to an increase in the amorphous phase and disorder. A decrease in the intensity of the diffracted peaks with the increase of dopant level was also reported in sol–gel synthesized Fe doped SnO_2 [32].

Diffraction analysis is a very important tool for studying the crystal growth of a nanoparticules. It allows us to calculate the size of crystallites which can play an important role in the physical properties (electrical, optical,…) of materials.

The grain sizes were evaluated from the width at mid-height (in 2θ) of the diffraction peak using Scherrer's formula [33]:

$$D = \frac{0.9\lambda}{\cos\theta} \qquad (1)$$

Where: λ = 1.54056Å, θ is the angle of incidence.

From relation (1) the Values a and c are calculated as follows:

$$d_{hkl} = \frac{a}{\sqrt{h^2 + k^2 + \left(l\frac{a}{c}\right)^2}} \qquad (2)$$

Table .1 represents the values of the grain size(D), *c/a* ratio, micro-strain (*ε*), dislocation (δ), specific surface area (S) and the lattice parameters “a” and “c” of SnO2, $Sn_{1-x}Fe_xO_2$ nanoparticles.

We valued the lattice constant ato lie between 4.7227 and 4.7269Å, while lattice constant c lies between 3.1878 and 3.1806Å, for undoped SnO_2 and $Sn_{0.90}Fe_{0.10}O_2$ respectively, which due to the substitution of iron in SnO_2. The c/a fraction decreases with the doping rate which

shows a progression in the basal plane, note that the decrease in unit cell volume with the rate doping confirms the insertion of Fe^{3+} in SnO_2 lattice which can be considered as a greater distortion of the cell.

Indeed, the size deduced by Scherrer's relation, It is obvious that calcination (600°C) can strengthen the crystallinity of the samples, but also increase the size of the crystallite grains, for the undoped sample with a value of 47 nm, while for doped samples the crystallite size was 27 nm for x = 0.02, 18 nm for x = 0.05, and 16 nm for x = 0.10, this decrease in crystallite size is clearly observed with the doping rate which confirms the substitution of Sn^{4+} by Fe^{3+} ions which is explained by their proximity to ion rays (0.72 Å for Sn^{4+} [34] and 0.64 Å for Fe^{3+} [35]), this substitution of Sn^{4+} by Fe^{3+} ions is very possible. It is probable that the relative 3+ oxidation state of the iron ions, which is already contained in the precursor used ($FeCl_3$-$6H_2O$), is mainly kept in the SnO_2 matrix [36,37]. It is clear that the addition of Fe blocked the progression of the SnO_2 crystal grains. Note that the decrease in unit cell volume with the rate doping confirms the insertion of Fe^{3+} in SnO_2 lattice which can be considered as a greater distortion of the cell.

The lattice strain, it iusually means the inhomogeneous local strain in the material which gives rise to x-ray peak broadening. It is only one factor causing peak broadening. The other factors are small crystallite size and presence of lattice defects.

The determination of the stresses produced in the nanoparticles due to lattice distortion and impurities was carried out using the Stoke Wilson formula [38]:

$$\varepsilon = \frac{\beta}{4\tan\theta} \qquad (3)$$

Pure SnO_2 shows a strain of 0.17×10^{-3} while with a doping (Fe) content of 2%, it increases to 0.3×10^{-3}, 0.45×10^{-3} with 5% doping, and 0.50×10^{-3} with 10% doping. The positive signs of the stress values correspond to tensile stress. These strain variants may occur due to the deformation generated in the samples at the time of thermal expansion in different directions. In addition, the crystallite size is reversed proportionally to the deformation, which implies that a change in the crystallite size will cause a variability of the deformation in the sample.

The dislocation density value (δ) represents the number of dislocation lines per unit volume of the crystal, which is the size of the defects in a crystal. In other words, the dislocation density value will show the degree of crystallinity of the nanoparticle profile.

$$\delta = \frac{1}{D^2} \qquad (4)$$

The result of the dislocation density (δnp) of the $Sn_{1-x}Fe_xO_2$[x=0, 2, 5 and 10 at%] nanoparticles is $0.444\times10^{-3}nm^{-2}$, 1.306×10^{-3} nm^{-2}, $2.929\times10^{-3}nm^{-2}$ and $3.631\times10^{-3}nm^{-2}$ respectively . Based on the results of this calculation is known that the dislocation density (δnp) of the nanoparticles obtained in this study is increase with increasing of rate doping wich indicates that SnO_2:Fe nanoparticles have been produced had a low degree of crystallinity because of presence of impurty (Fe). which confirmed the presence of Fe^{3+} ions in the SnO_2 lattice.

3.2 Morphological properties: SEM

Scanning Electron Microscope (SEM) observations have also been carried out. on all synthesized nanocatalysts in order to evaluate the evolution of crystallite morphology and size. SEM characterizations were performed at two magnifications for all synthesized pure SnO2 and Fe-doped powders. The images in Figure 2, show the presence of nanoparticle agglomerates consisting of crystallites of mainly quasi-spherical shape with a relatively small and homogeneous particle size distribution.

3.3 EDS characterization

The EDS spectra of the chemical composition of our Fe-doped SnO_2 layers are as follows represented in figures 3. The analysis by energy dispersive X-ray spectroscopy (EDS) allowed us to verify the chemical composition of nanoparticles. All spectra show an apparent presence of tin and oxygen. The main objective of using this technique (EDS) is the confirmation of the existence of Fe. All the spectra show the presence of this element, coming from doping and we have noticed an increase in the intensity of the iron peak with the increase in the rate of doping.

The stoichiometric of the $Sn_{1-x}Fe_xO_2$ nanostructure is measured exclusively from the Fe and Sn signals. According to the following relation (Eq. (5)) [39,40]:

$$x = \frac{r}{(1+r)} \qquad (5)$$

Where x represents the Fe atom content and r the ratio of the Sn and Fe EDS signals (see Table 2).

Figure 4a, b show the variation of the ratio between the EDS signals of Fe and Sn as well as the calculated value atomic Fe content, both plotted against the "expected" Fe content of the deposit. The incorporation of Fe in the high network is very clear, for all doping concentrations

3.4 FTIR Spectroscopy

The study by FTIR spectroscopy performed on the different samples (in the wavelength range from 400 to 4000 cm-1) is presented in figure 5, the absorption bands are recorded for wavelengths 3436, 1628, 1254, 1022 and 620 cm^{-1}. The large vibrations existing at 3436 cm^{-1} and 1628cm^{-1} indicate the presence of hydrogen bonds involved in O-H oscillators. The peaks at 1623 cm^{-1} correspond to the O-H bending bonds associated with some residual water molecules, while small peaks around 1022 cm^{-1} and 1254 cm^{-1}, have also been recorded and can be attributed to hydrogen bonds involved in O-H oscillators. The vibration of the antisymmetric functional groups of the SnO_2, O-Sn-O bridge presents about 620 cm^{-1} [41].

3.5 UV-Vis-NIR spectroscopy

The synthesized nanoparticles were analyzed by UV-Vis-NIR spectroscopy in the 300-700nm wavelength region. Fig. 6 shows the optical absorbance spectra of SnO_2, $Sn_{1-x}Fe_xO_2$[x=0, 2, 5 and 10 at%] nanoparticles.

The absorption edge position is located between 364 nm and 375nm depending on the Fe content. The ultraviolet cut-off we notice can be due to the photo-excitation of electrons from the valence band to the conduction band, specifies the electronic transition from the valence band O^{2-} (2p) to the conduction band Sn^{4+} (5p), i.e. the direct recombination of holes and electrons in the valence and conduction bands of O-2p and Sn-5p respectively.

The absorption value decreases with doping and minimizes at Fe = 10%. During Fe substitution, the absorption edge is shifted to the higher wavelength side. The nanoparticle absorption is expected to be related to various factors such as particle size, band gap, defects and impurity centers.

The higher absorption intensity at Fe = 5% is due to the distortion caused by the Fe ions in the $Sn0_2$ lattice. In addition, the higher absorption in the lower wavelength region (300-350 nm) is accompanied by a higher absorption in the visible region. This higher UV absorption at Fe = 5% is the result of the improved transition of electrons from the valence band to the conduction band and a decrease in the size of the crystallites (size effect) is noted in this case.

The Optical Transmittance Spectra of Fe-doped SnO_2 nanoparticles from 300 nm to 700 nm are shown in Fig. 7. It can be seen that the sample doped with Fe = 5% has a lower transmittance value and the sample doped with Fe = 10% has a higher transmittance value. A higher optical absorption or lower transmittance may be due to the optical transitions from the 3d occupied band to the 4s-4p band of Fe point defects.

On the nanoscale, the band gap increases with the reduction of the size of the nanoparticles due to the quantum confinement effect, which generates discrete energy levels in the valence band and the conduction band. As the energy band gap increases, the restriction of electron movement increases. This shifts the absorption peak to lower wavelengths, i.e. to the blue region.

The direct optical band gap (Eg) of Sn1-xFexO2 nanoparticles can be determined from the absorption coefficient (α) and photon energy (hν) by the following relation [42]:

$$\alpha h\nu = A\left(h\nu - E_g\right)^n \quad (6)$$

Where A is a constant, Eg is optical band gap of the material and the exponent n depends upon the direct/indirect allowed transition. In the present case, n is taken as ½ because of allowed direct transition. The curves have been plotted as αhν Vs hν for all the samples as exposed in Figure 8. The Eg value for undoped SnO2 is 3.6 eV, which is in good accord with the previously reported values [43], the incorporation of Fe ions into the host SnO2 decreased the band gap energy. The energy band gap reduced to 3.30 eV for 2% doping and then increased to 3.35 eV and 3.40 eV with an augmentation of the doping level by 5% and 10% respetively. These alterations in the band gap as dependent on the doping amount can be related to the increase in the defects of oxygen vacancies in the lattice. These defects result in impurity energy states in the band gap where the holes trap free electrons in the valence band and, as a consequence of instability, they will recombine with the holes in the conduction band, which results in a reduction of the band gap. Thus, the change in the energy band gap is a function of oxygen deficiency and lattice distortion generated as a response to the change in doping content in the host material.

The absorption spectra show a continuous red shift with increasing Fe content.The band gap energy decreases and the absorption edge increases with Fe content, is interpreted to

incorporation of Fe3+ into SnO2 NPs [44,45]. It was assigned to the charge transfer transitions between the d-electrons of Fe3+ and the conduction or valence band of SnO2 [44] and to the the reduction of the size of the nanoparticles

3.6 Photocatalytic activity

The evolution of the UV spectra of solutions irradiated from BM (8×10^{-3}M) at 250 nm in the presence of $Sn_{0.95}Fe_{0.05}O_2$ photocatalyst as a function of the irradiation time (Figure. 9) shows essentially a decrease of the optical density at the absorption maximum of MB at 664 nm. Images of MB samples irradiated in the presence of the $Sn_{0.95}Fe_{0.05}O_2$ photocatalyst after 3 hours clearly show the progressive discoloration of the pollutant compared to the initial non-irradiated sample. The rate in Fig.10 represents the ratio between the amount of reagent processed and the initial amount, using the following equation:

$$D_t(\%) = \frac{A_0 - A_t}{A_0} \times 100 \quad (7)$$

Where A_0 is the initial absorbance of the dye, A_t the absorbance of the dye in solution at time t

Figure .11 shows that irradiation leads to a progressive discoloration of the MB. A reduction of about 65% is observed after 3hours of irradiation, the kinetics of the degradation reaction of methylene blue in Solution, and he calculated kinetic parameters of MB degradation are shown in Table 3, according to the equation [46].

$$A=X*\exp(-k*t)+E \quad (8)$$

While the unit of (pseudo-) order rate constant k is the inverse of the unit of time used (min^{-1}), X is the amplitude of the process, E is the endpoint, both of them have the same units as the measured quantity A. The photodegradation was linear (R^2 = 0.9513), following an apparent kinetics of order 1 with an apparent speed constant of 0.0358 min^{-1}.

The reaction path for the degradation of methylene blue (MB) using $Sn_{0.95}Fe_{0.05}O_2$ fine nanopowders under UV irradiation is as follows:

$$h_{VB}^{+} + H_2O \rightarrow OH^{+} + \cdot OH \quad (9)$$

$$h_{VB}^{+} + OH^{-} \rightarrow \cdot OH \quad (10)$$

$$e_{CB}^{-} + O_2 \rightarrow \cdot O^{-2} \quad (11)$$

$$e_{CB}^{-} + \cdot O^{-2} + 2H^{+} \rightarrow H_2O_2 \quad (12)$$

$$H_2O_2 + \cdot O^{-2} \rightarrow \cdot OH + OH^{-} + O_2 \quad (13)$$

Several factors influence the photocatalytic activity of $Sn_{0.95}Fe_{0.05}O_2$ fine nanopowder, namely, the morphology of the nanoparticles, as well as the porosity of the nanoparticles. In addition, it has been reported that increasing the specific surface area by reducing the size of SnO_2 crystallites also increases the efficiency of photocatalysis [47], which could provide more active sites for BM molecules and thus promote the efficiency of electron-hole separation.

The specific surface area of the samples was obtained using equation (14) [48]:

$$S = \frac{6}{\rho D} \quad (14)$$

S: the specific surface area of the nanoarticules.

D: the average size of crystals.

ρ : the density of the material.

The increase in photocatalytic activity of fine nanopowder $Sn_{0.95}Fe_{0.05}O_2$ may be due to the increase in the number of crystal defects. In other terms, the network distortion ($0{,}45\times10^{-3}$) and dislocation density ($2{,}929\times10^{-3}nm^{-2}$) relative to the to undoped samples resulted in a reduction in particle size (18.47nm). This led to an increase in the specific surface area (46.74 $m^2 .g^{-1}$, Table. 1), this last parameter contributes very favourably in the degradation photocatalytic of pollutants in general and that of MB in our particular case.

It should also be noted that the shift of the optical gap of $Sn_{0.90}Fe_{0.05}O_2$ doped nanoparticles towards longer wavelengths (Red Shift) [49], leads to a decrease of the electron-hole recombination, thus producing a more efficient separation of the photogenerated pairs and consequently prolonging the life time of electrons and holes on the surface of SnO_2 doped nanowires.

4. Conclusion

In this work, nanoparticles of photosensitive SnO_2, $Sn_{1-x}Fe_xO_2$ [x=2. 5 and 10 at%] were synthesized, characterized and then used in photocatlytic applications. The nanomaterials, pure tin dioxide and iron-doped tin dioxide at different concentrations, were synthesized by a simple and classical "co-precipitation" method. The aim is to obtain materials with controlled properties, especially with regard to crystallite size, morphology and especially optical properties which play a very important role in photocatlytic applications.

All the X-ray diffraction spectra of our samples showed a polycrystalline growth and all peaks observed correspond to the rutile tetragonal structure of SnO_2. The crystallite size of the layers calculated by the Debye-Scherrer method is 47.41 to 16.59 nm, the incorporation of Fe atoms in the SnO_2 matrix in substitution creates pressures in the crystal lattice and leads to a deterioration of the crystal quality of the doped SnO_2 nanoparticles.

The SEM characterization provided information on the morphology of surface of the processed nanoparticles. In the nanoparticles of SnO_2, SnO_2: Fe, the grains have quasi-spherical shapes with different sizes and uneven distribution on the surface. The growth mechanism of these crystallites involves the aggregation of atoms with each other to form nucleation centers. UV-vis results indicate that the band gap of SnO_2 NPs decrease with Fe doping.

The presence of dopant in the SnO2 nanoparticles prevented the growth of these crystallites, so they appear smaller and denser compared to the pure SnO2 film. The irregularity of the surface of the doped (5%) Fe SnO_2 nanoparticles also provided nucleation sites through pores and cracks.

This result makes the (5%) Fe doped SnO_2 sample potentially more suitable for photocatlytic applications. The nanoparticles of SnO_2 doped (5%) Fe exhibited higher photocatlytic activity with UV irradiation compared to those of pure SnO_2 with respect to degradation of the methylene blue dye.

Funding statement: No funding

Acknowledgments: The authors would like to thank the National Project Research (PNR) and LASPI^{2}A Laboratory of Khenchela University (Algeria) for their financial support of this

research project. The authors thank Pr. Abdecharif Boumaza for FTIR analysis, Laboratoire des Structures, Propriétés et Interactions Inter Atomiques (LASPI2A), Université Abbes Laghrour, 40000 Khenchela, Algeria.

Author contributions: The manuscript was written through contributions of all authors. All authors have given approval to the final version of the manuscript.

Compliance with ethical standards

Conflict of interest: No conflict of interest exits in the submission of this manuscript, and manuscript is approved by all authors for publication. The work described is original research that has not been published previously, and is not under consideration for publication elsewhere, in whole or in part**.**

.

Reference

1. A. San-Miguel, Nanomaterials under high-pressure. Chem. Soc. Rev. 35, 876-889 (2006).
2. D.P. Otto, M.M. De Villiers, Why is the nanoscale special (or not) ? Fundamental properties and how it relates to the design of nano-enabled drug delivery systems. Nanotechnol. Rev. 2, 171-199 (2013)
3. F. Zaera, Nanostructured materials for applications in heterogeneous catalysis. Chem. Soc. Rev. 42, 2746-2762 (2013) .
4. J. Kaur, J. Shah, R.K. Kotnala, K.C. Verma, Raman spectra, photoluminescence and ferromagnetism of pure, Co and Fe doped SnO2 nanoparticles. Ceram. Int. 38,5563-5570 (2012).
5. W. Wei, Y. Dai, B. Huan, Role of Cu Doping in SnO2 Sensing Properties Toward H2S . J.Phys.Chem.C. 115,18597-18602 (2011) .
6. M. Batzill, U. Diebold , The surface and materials science of tin oxide. Prog.Surf. Sci. 79, 47-154 (2005).
7. J. Hays, A. Punnoose, R. Baldner, M. H. Engelhard, J. Peloquin, K. M. Reddy , Relationship between the structural and magnetic properties of Co-doped SnO2

nanoparticles. Phys. Rev. B.72, 075203 (2005).

8. S. J. Ding,et al, Formation of SnO2 Hollow Nanospheres inside Mesoporous Silica Nanoreactors. J. Am. Chem. Soc. 133, 21-23 (2011).
9. D. Deng, J. Y. Lee , Hollow Core–Shell Mesospheres of Crystalline SnO2 Nanoparticle Aggregates for High Capacity Li+ Ion Storage. Chem. Mater. 20,1841-1846 (2008).
10. W.I. Park, D.H. Kim, S.W. Jung, G.C. Yi , Metalorganic vapor-phase epitaxial growth of vertically well-aligned ZnO nanorods. Appl. Phys. Lett. 80,4232. (2002)
11. W.I. Park, D.H. Kim, G.C. Yi, S.J. Pennycook , Park W. Il, G.C. Yi, M. Kim, S.J. Pennycook, ZnO nanoneedles grown vertically on Si substrates by non-catalytic vapor-phase epitaxy. Adv. Mater. 14, 1841–1843 (2002).
12. J.J.Wu, S.C. Liu, Catalyst-Free Growth and Characterization of ZnO Nanorods . J Phys. Chem. B 106, 9546–9551(2002).
13. N. Bhardwaj, A. Pandey, B. Satpati, M. Tomar, V. Guptae, S. Mohapatra, Enhanced CO gas sensing properties of Cu doped SnO_2 nanostructures prepared by a facile wet chemical method. PCCP. 18, 18846-18854 (2016).
14. M.S. Arnold, P. Avouris, Z.W. Pan, Z.L. Wang, Field-Effect Transistors Based on Single Semiconducting Oxide Nanobelts. J. Phys. Chem. B. 107,659-663 (2003).
15. Z.R. Dai, Z.W. Pan, Z.L. Wang , Growth and Structure Evolution of Novel Tin Oxide Diskettes. J. Am. Chem. Soc.124, 8673-8680 (2002).
16. J. Kaur, J. Shah R.K. Kotnala, K. Ch. Verma, Raman spectra, photoluminescence and ferromagnetism of pure, Co and Fe doped SnO2 nanoparticles. Ceram. Int. 38, 5563-5570 (2012).
17. A.F. Cabrera, A.M.M. Navarro, C.E.R. Torres, F.H. Sanchez, Mechanosynthesis of Fe-doped SnO2 nanoparticles. Phys. B: Condens. Matter. 398, 215-218 (2007).
18. T.N. Soitah, C. Yang, L. Sun , Structural, optical and electrical properties of Fe-doped SnO2 fabricated by sol–gel dip coating technique. Mater. Sci. Semicond. Process. 13, 125-131 (2010).

19. R.K. Mishra, A. Kushwaha, P.P. Sahay , Influence of Cu doping on the structural, photoluminescence and formaldehyde sensing properties of SnO2 nanoparticles .RSC Adv. 4, 3904-3912 (2014).
20. F.Du, Z. Guo, G. Li , Hydrothermal synthesis of SnO2 hollow microspheres. Materials Letters. 59,2563-2565 (2005).
21. Y.Liu, E. Koep, M. Liu, A Highly Sensitive and Fast-Responding SnO2 Sensor Fabricated by Combustion Chemical Vapor Deposition. Chem. Mater. 17, 3997-4000 (2005).
22. F. Pourfayaz, A. Khodadadi, Y. Mortazavi, S.S. Mohajerzadeh , CeO2 doped SnO2 sensor selective to ethanol in presence of CO, LPG and CH4.Sens. Actuators B. 108, 172-176 (2005).
23. J.D.Castillo, V. D. Rodriguez, A. C. Yanes, J. Mendez-Ramos, M.E. Torres , Luminescent properties of transparent nanostructured Eu^{3+} doped SnO_2–SiO_2 glass-ceramics prepared by the sol–gel method. Nanotechnology. 16, S300 (2005).
24. H. Zhu, D. Yang, G. Yu, H. Zhang, K. Yao , A simple hydrothermal route for synthesizing SnO_2 quantum dots. Nanotechnology. 17, 2386 (2006).
25. P. Venkateswara Reddy, S. Venkatramana Reddy, B. Sankara Reddy , Synthesis and properties of (Fe, Al) co-doped SnO2 nanoparticles. Materials Today: Proceedings. 3,1752-1761 (2016).
26. Y. Kumar, et al , Controlling of ZnO nanostructures by solute concentration and its effect on growth, structural and optical properties. Materials Research Express. 2, 105017 (2015).
27. Rana et al, Growth of transparent Zn1−xSrxO ($0.0 \leq x \leq 0.08$) films by facile wet chemical method: Effect of Sr doping on the structural, optical and sensing properties. Applied Surface Science 379,23–322016.
28. P.M. Shirage, A.K . Rana, Y. Kumar, S. Sen, S. G. Leonardi, G. Neri , Sr- and Ni-doping in ZnO nanorods synthesized by a simple wet chemical method as excellent materials for

CO and CO2 gas sensing. RSC Advances. 6, 82733-8274286 (2016).

29. A.K. Singh, A. Janotti, M. Scheffler, C.G. Van de Walle , Sources of Electrical Conductivity in SnO2. Phys. Rev. Lett. 101, 055502 (2008).
30. Ch.Y. Tsay, Sh.Ch. Liang , Fabrication of p-type conductivity in SnO2 thin films through Ga doping. J. Alloy Compd. 622, 644-650 (2015).
31. C.E. Benouis, et al , The low resistive and transparent Al-doped SnO2 films: p-type conductivity, nanostructures and photoluminescence. J. Alloy Compd. 603, 213-223 (2014).
32. K. Nomura, C.A. Barrero, J. Sakuma, M. Takeda , Room-temperature ferromagnetism of sol-gel-synthesized Sn1−x 57FexO2− powders. Phys. Rev. B. 75,184411 (2017).
33. R. Anandhi, R. Mohan, K. Swaminathan, K. Ravichandran , Influence of aging time of the starting solution on the physical properties of fluorine doped zinc oxide films deposited by a simplified spray pyrolysis technique. Superlattices Microstruct. 51,680-689 (2012)
34. S.J. Hu, S.S. Yan, X.X. Yao, Y.X. Chen, G.L. Liu, L.M. Mei, Electronic structure and magnetic properties of Fe0.125Sn0.875O2. Phys. Rev. B. 75, 094412 (2007).
35. M.M. Bagheri-Mohagheghi, N. Shahtahmasebi, M.R. Alinejad, A. Youssefi, M. Shokooh-Saremi, Fe-doped SnO2 transparent semi-conducting thin films deposited by spray pyrolysis technique: Thermoelectric and p-type conductivity properties. Solid State Sci. 11, 233-239 (2009).
36. A. Punnoose,et al, Dopant spin states and magnetism of Sn1xFexO2 nanoparticles. J. Appl. Phys. 115, 17B534 (2014).
37. V. Bilovol, C. Herme, S. Jacobo, A.F. Cabrera, Study of magnetic behaviour of Fe-doped SnO2 powders prepared by chemical method. Mater. Chem. Phys. 135, 334-339 (2012).
38. G. J. Wilson, Aaron S. Matijasevich, D. R G Mitchell, J. C. Schulz, and G. D. Will, Modification of TiO2 for Enhanced Surface Properties: Finite Ostwald Ripening by a

Microwave Hydrothermal Process. Langmuir. 22, 2016-2027 (2006).

39. S.Roguai, A.Djelloul, A structural and optical properties of Cu-doped ZnO flms prepared by spray pyrolysis. Applied Physics A. 126 , ,122 (2020).

40. S. Roguai, A. Djelloul A , Synthesis and evaluation of the structural, microstructural, optical and magnetic properties of Zn1−xCoxO thin flms grown onto glass substrate by ultrasonic spray pyrolysis. Applied Physics A. 125, 816 (2019).

41. J. Kaur, J. Shah, R.K. Kotnala, K.C. Verma , Raman spectra, photoluminescence and ferromagnetism of pure, Co and Fe doped SnO2 nanoparticles. Ceram. Int. 38, 5563-5570 (2012).

42. R. Sangeetha, S. Muthukumaran, M. Ashokkumar, Spectrochim. Acta Part A: Mol. Biomol. Spectrosc. 144, 1-7 (2015).

43. C.M. Liu, X.T. Zu, Q.M. Wei, L.M. Wang, Fabrication and characterization of wire- like SnO2. J. Phys. D. 39, 2494-2497 (2006)

44. S. J. Rani, S. C. Roy, N. Karar and M. C. Bhatnagar, Structure, microstructure and photoluminescence properties of Fe doped SnO2 thin films. Solid State Commun. 141, 214-218 (2007)

45. S. J. Hu, S. S. Yan, X. X. Yao, Y. X. Chen, G. L. Liu and L. M. Mei, Electronic structure and magnetic properties of $Fe_{0.125}Sn_{0.875}O_2$. Phys. Rev. B. 75, 094412 (2007)

46. Gábor Lente: Deterministic Kinetics in Chemistry and Systems Biology. Springer. ISBN 978-3-319-15481-7,52 (2015)

47. X.Y. Kong, Y. Ding, R. Yang, Z.L. Wang, Single-Crystal Nanorings Formed by Epitaxial Self-Coiling of Polar Nanobelts. Science, 303, 1348-1351 (2004).

48. F. Rataboul, C. Nayral , M. Casanove , A. Maisonnat, B. Chaudret , Synthesis and characterization of monodisperse zinc and zinc oxide nanoparticles from the organometallic precursor [Zn(C6H11)2].J. of Organometallic. Chem. 643-644, 307-312 (2002).

49. W.Ben Haj Othmen ,et al, Iron addition induced tunable band gap and tetravalent Fe ion in hydrothermally prepared SnO2 nanocrystals: Application in photocatalysis. Materials Research Bulletin 83, 481–490 (2016).

Table Captions

Table 1 X-ray diffraction data (grain size(D), *c*/*a* ratio, micro-strain (ε), dislocation (δ), specific surface area (S) and the lattice parameters "a" and "c") of different $Sn_{1-x}Fe_xO_2$ nanoparticles.

Table 2 Dispersion parameters of the $Sn_{1-x}Fe_xO_2$ nanoparticles extracted by fitting the experimental data.

Table 3. Pseudo-first-order kinetic parameters of MB degradation.

Figure Captions

Figure. 1 XRD patterns of SnO_2 and $Sn_{1-x}Fe_xO_2$ (with x = 2, 5 and 10 at%) nanoparticles

Figure. 2 SEM images of $Sn_{1-x}Fe_XO_2$ [x=0, 2, 5 and 10 at%] nanoparticles.

Figure. 3 EDX elemental composition analysis of a pure SnO_2 nanoparticles and b–d Fe–doped $Sn_{1-x}Fe_XO_2$ [x= 2,5 and 10] nanoarticles.

Figure. 4 a The measured Fe/Sn atomic ratio and **b** the calculated Fe atomic content (from EDS analysis) plotted as function of the expected Fe content/doping

Figure. 5 FTIR spectra of $Sn_{1-x}Fe_XO_2$ [x=0, 2, 5 and 10 at%] nanoparticles at room temperature in the wave number from 400 to 4000 cm^{-1}

Fig. 6. UV–Visible absorption spectra of $Sn_{1-x}Fe_XO_2$ [x=0, 2, 5 and 10 at%] nanoparticles.

Fig. 7. Transmittance spectra of of $Sn_{1-x}Fe_XO_2$ [x=0, 2, 5 and 10 at%] nanoparticles.

Fig. 8. The $(\alpha h\nu)^2$ versus $h\nu$ curves of of $Sn_{1-x}Fe_XO_2$ [x=0, 2, 5 and 10 at%] nanoparticles, for the optical energy gap calculation.

Figure. 9 The effect of $Sn_{0.95}Fe_{0.05}O_2$ nanoparticles on the absorption spectra of MB solution for different reaction time under UV irradiation.

Figure. 10 Degradation rate of $Sn_{0.95}Fe_{0.05}O_2$ nanoparticles in MB degradation

Figure. 11 Decolorization kinetics of MB aqueous solutions by $Sn_{0.95}Fe_{0.05}O_2$ nanoparticles without UV irradiation. The nanoparticles were prepared by using co-precipitation method. The photocatalytic process at UV-irradiation follows first-order kinetics according to the equation A=X*exp(-k*t)+E (cercles) Experimental data point and (solid lines) fitted curve (solid lines). Here A0 is the initial absorbance of the dye solution, A(t) is the absorbance at time t, and k is the rate constant of photocatalysis.

Table 1

Sample	Crystallite Size (nm)	Lattice Parameters (Å)	c/a ration	Unit cell volume (Å^3)	$\delta\times10^{-3}$ (nm^{-2})	$\varepsilon\times10^{-3}$	S (m^2/g)
SnO_2	47.41	*a* = 4.7227 *c* = 3.1878	0.6749	71 .100	0.444	0.17	18.20
$Sn_{0.88}Fe_{0.02}O_2$	27.66	*a* = 4.7233 *c* = 3.1817	0.6736	70.982	1.306	0.30	31.21
$Sn_{0.85}Fe_{0.05}O_2$	18.47	*a* = 4.7026 *c* = 3.1848	0.6772	70.430	2.929	0.45	46.74
$Sn_{0.90}Fe_{0.10}O_2$	16.59	*a* = 4.7269 *c* = 3.1806	0.6728	71.066	3.631	0.50	52.03

Table 2

$Zn_{1-x}Fe_xO$ “Nominal” Fe content (at)	Sn (at.%)	Fe (at.%)	O (at.%)	*x* (Fe) “EDS” Cu content (at)
SnO_2	34.47	/	65.53	0
$Sn_{0.98}Fe_{0.02}O_2$	37.54	1.01	61.46	0 .0262
$Sn_{0.95}Fe_{0.05}O_2$	36.83	2.39	60.78	0.0609
$Sn_{0.90}Fe_{0.10}O_2$	37.40	5.35	57.26	0.1251

Table 3

Samples	Value			Standard deviation			R^2
	$K(min^{-1})$	X	E	$K(min^{-1})$	X	E	
$Sn_{0.95}Fe_{0.05}O_2$	0.0358	0.6023	0.3876	0.0108	0.0689	0.0404	0.9513

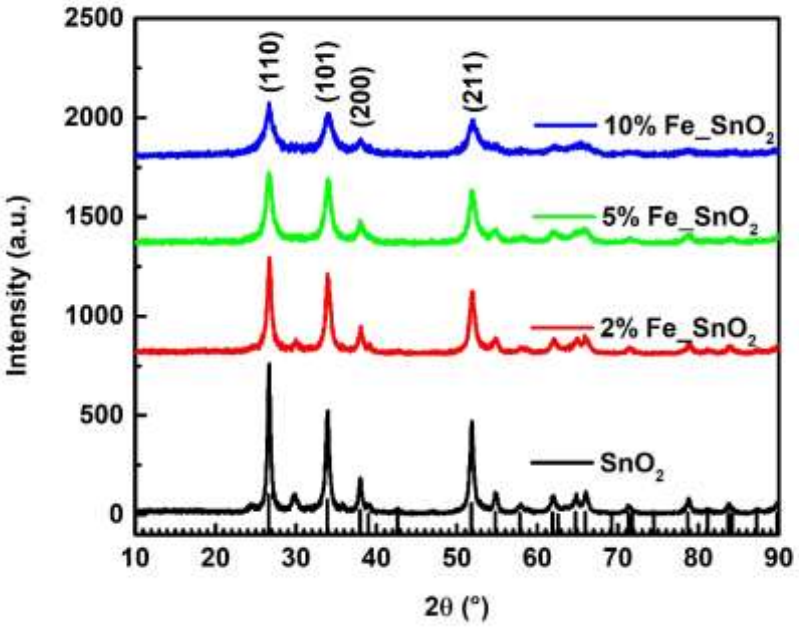
2500
2000
1500
1000
500
0
Intensity (a.u.)
10
20
30
40
50
60
70
80
90
2θ (°)
(110)
(101)
(200)
(211)
10% Fe_SnO2
5% Fe_SnO2
2% Fe_SnO2
SnO2

Fig. 1

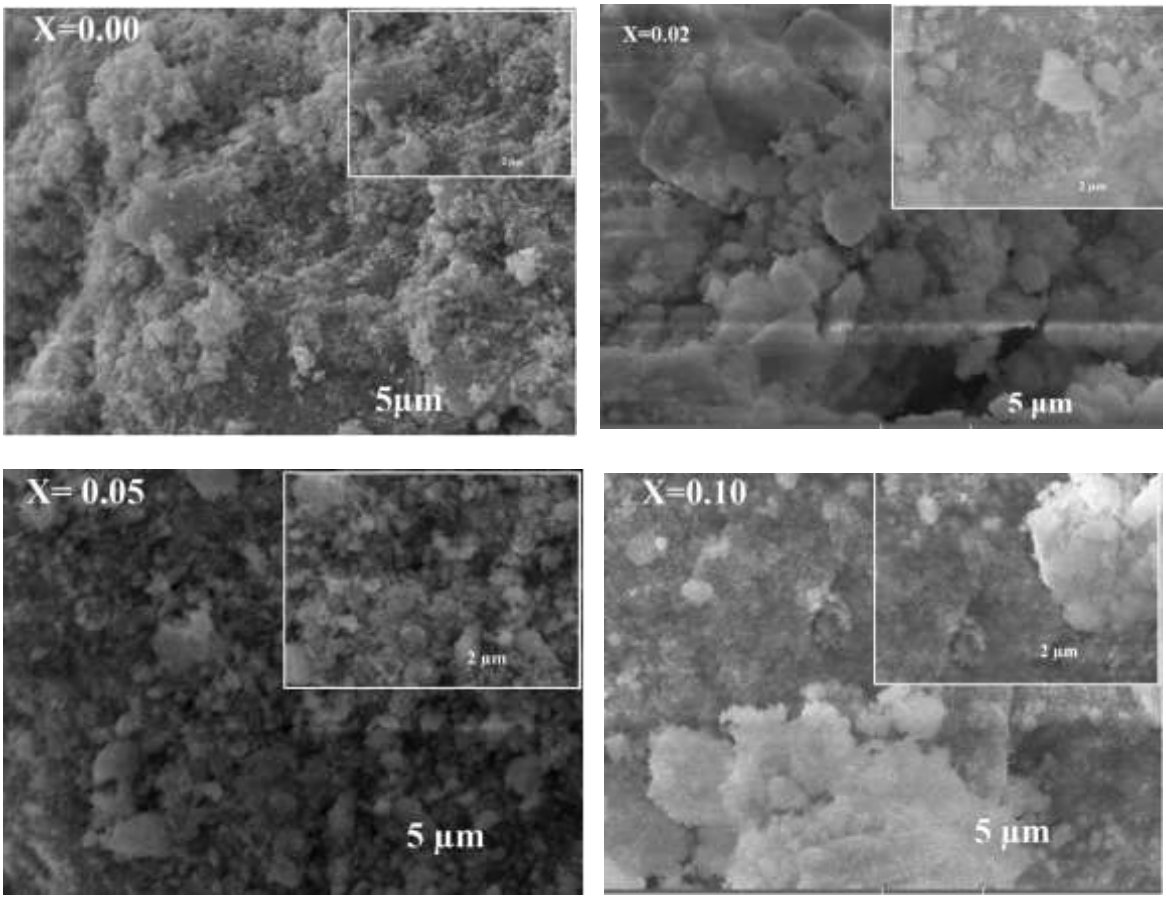

Fig. 2

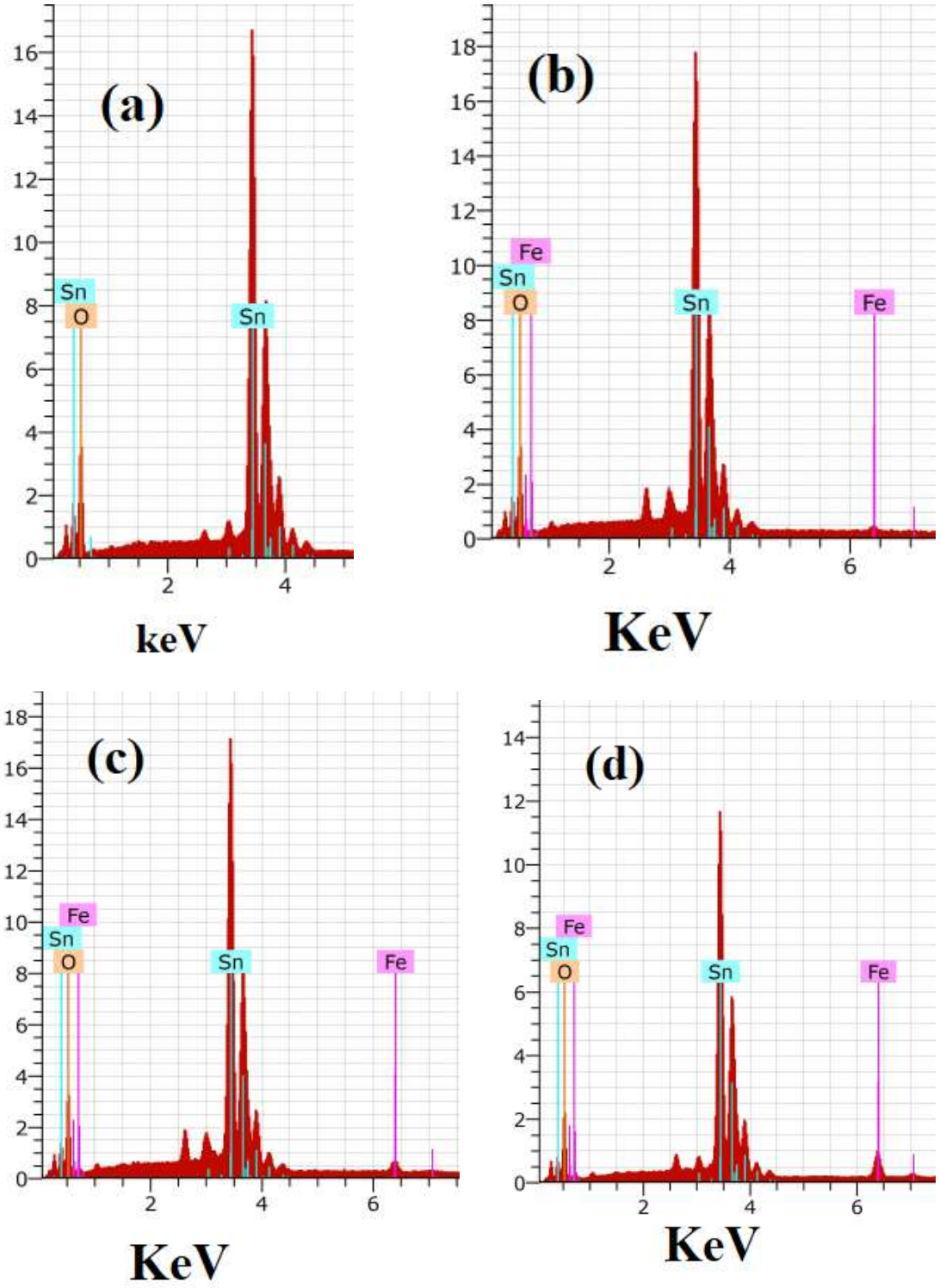

Fig. 3

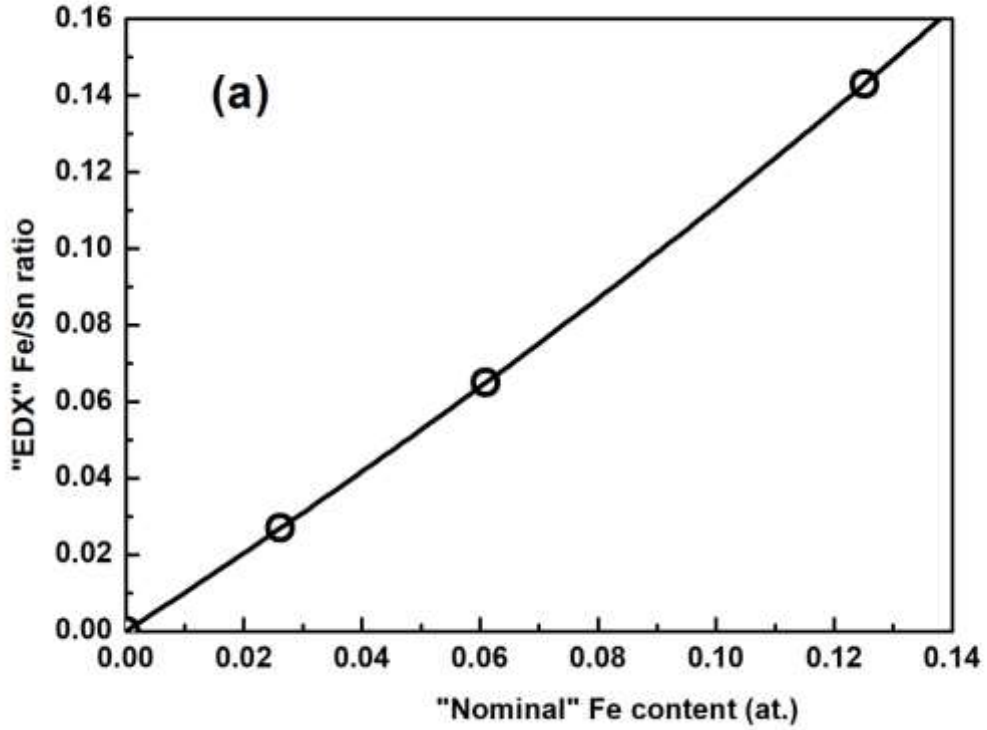
(a)
"EDX" Fe/Sn ratio
"Nominal" Fe content (at.)
0.00
0.02
0.04
0.06
0.08
0.10
0.12
0.14
0.16

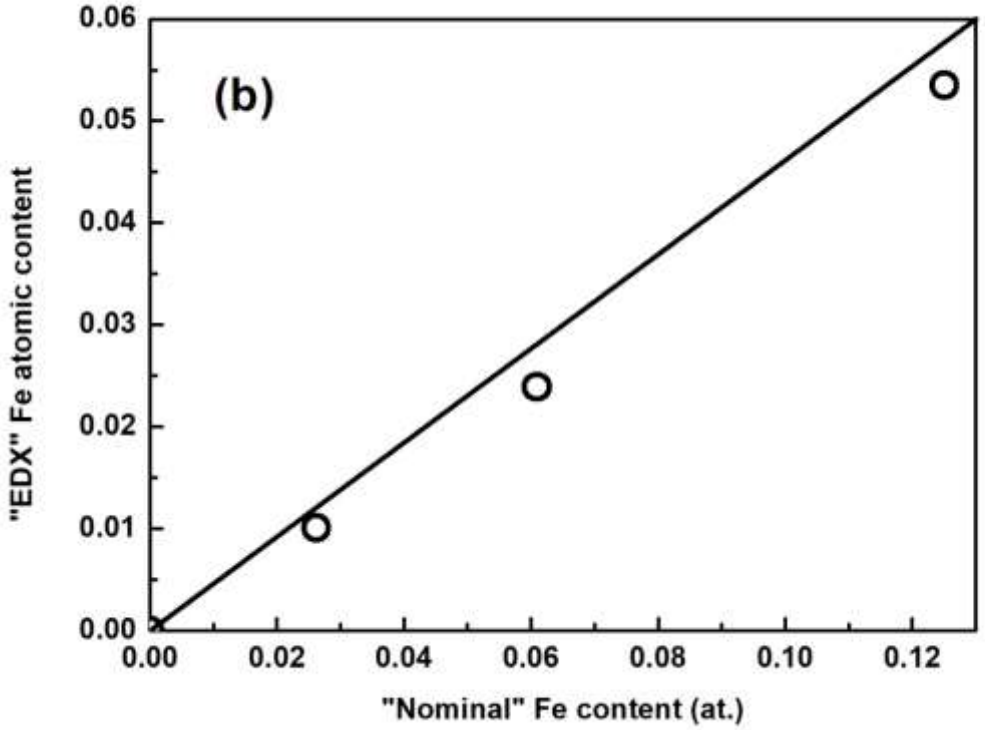
(b)
"EDX" Fe atomic content
"Nominal" Fe content (at.)
0.00
0.01
0.02
0.03
0.04
0.05
0.06
0.00
0.02
0.04
0.06
0.08
0.10
0.12

Fig. 4

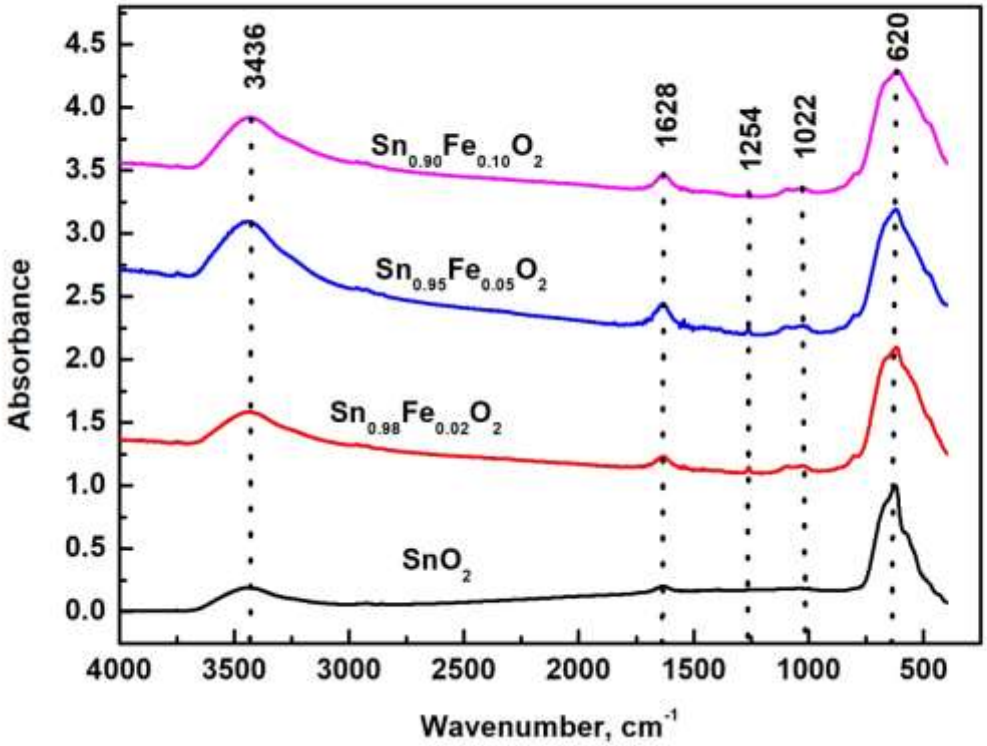
3436
1628
1254
1022
620
$Sn_{0.90}Fe_{0.10}O_2$
$Sn_{0.95}Fe_{0.05}O_2$
$Sn_{0.98}Fe_{0.02}O_2$
SnO_2
Absorbance
Wavenumber, cm^{-1}
4.5
4.0
3.5
3.0
2.5
2.0
1.5
1.0
0.5
0.0
4000
3500
3000
2500
2000
1500
1000
500

Fig. 5

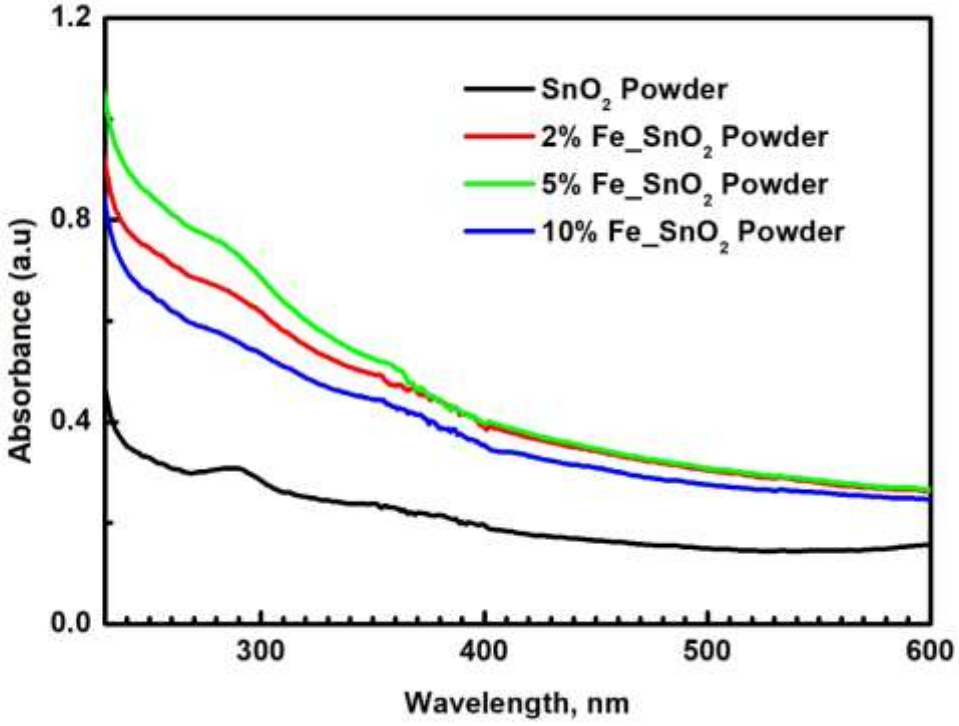
1.2
0.8
0.4
0.0
Absorbance (a.u)
300
400
500
600
Wavelength, nm
SnO2 Powder
2% Fe_SnO2 Powder
5% Fe_SnO2 Powder
10% Fe_SnO2 Powder

Fig.6

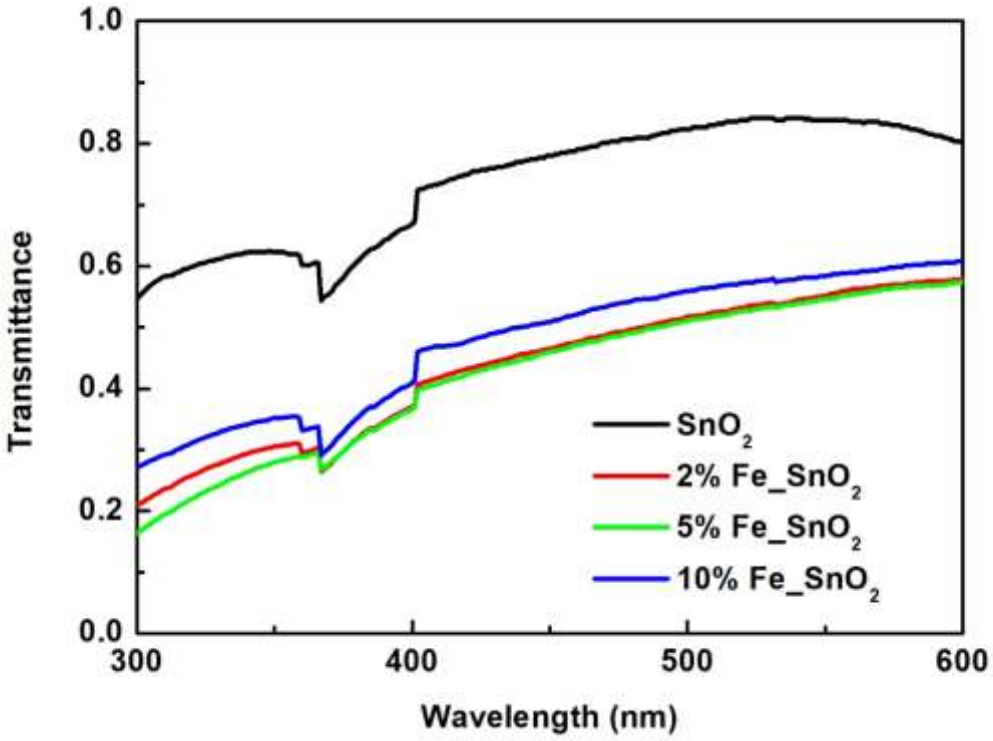
Transmittance
1.0
0.8
0.6
0.4
0.2
0.0
300
400
500
600
Wavelength (nm)
SnO2
2% Fe_SnO2
5% Fe_SnO2
10% Fe_SnO2

Fig.7

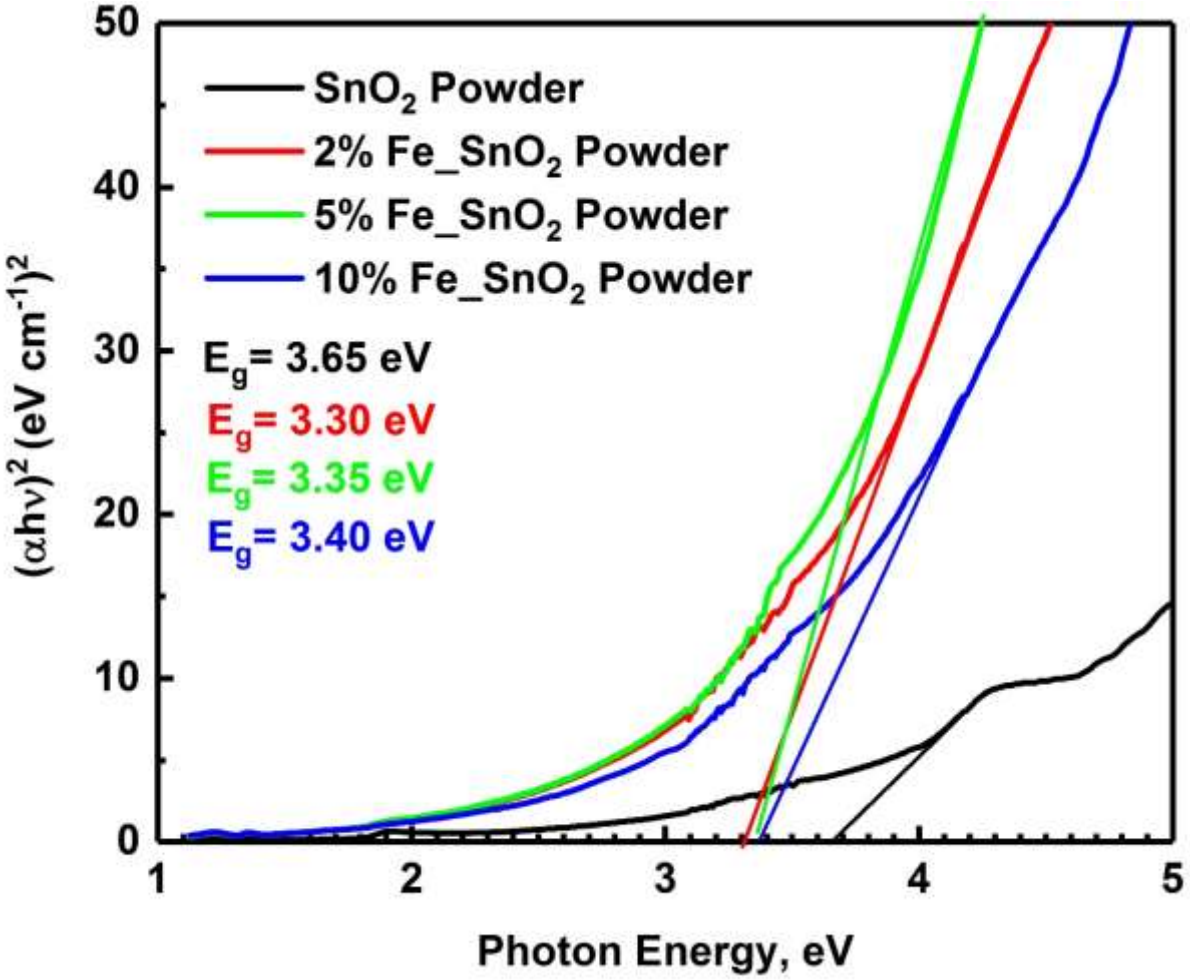
SnO2 Powder
2% Fe_SnO2 Powder
5% Fe_SnO2 Powder
10% Fe_SnO2 Powder
Eg= 3.65 eV
Eg= 3.30 eV
Eg= 3.35 eV
Eg= 3.40 eV
(αhν)2 (eV cm-1)2
Photon Energy, eV
0
10
20
30
40
50
1
2
3
4
5

Fig.8

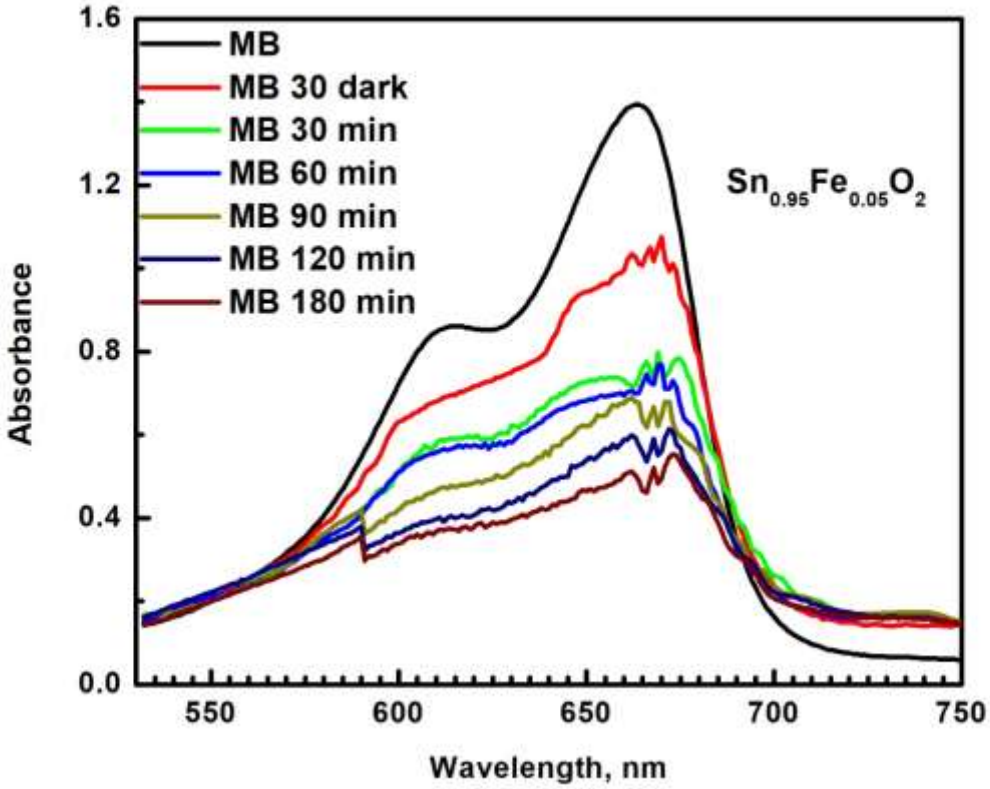
MB
MB 30 dark
MB 30 min
MB 60 min
MB 90 min
MB 120 min
MB 180 min
Sn0.95Fe0.05O2
Absorbance
Wavelength, nm
1.6
1.2
0.8
0.4
0.0
550
600
650
700
750

Fig. 9

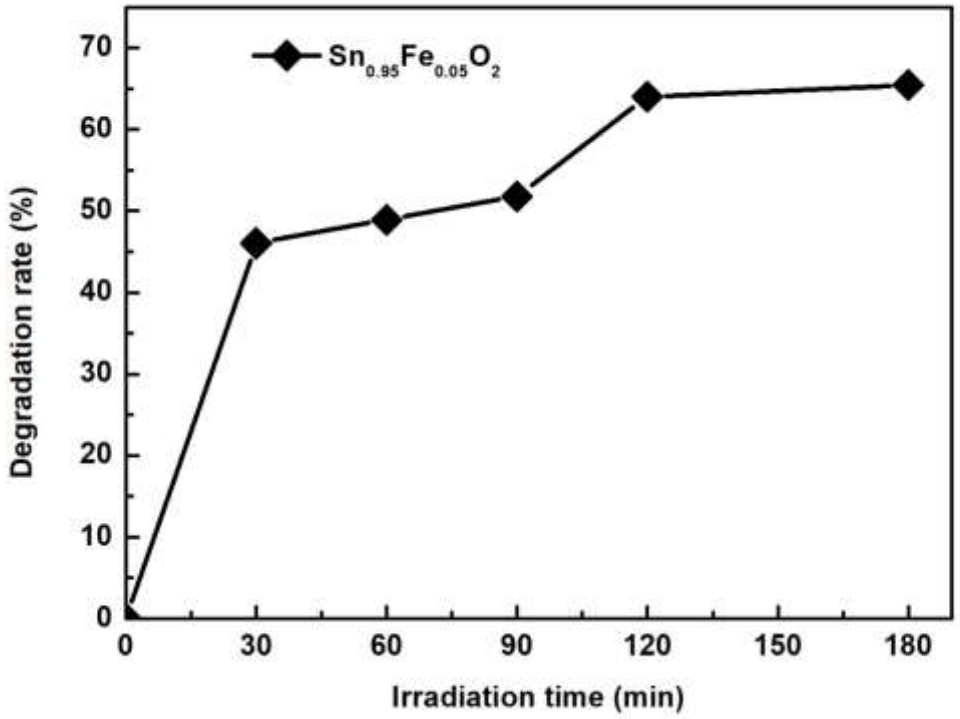
Sn0.95Fe0.05O2
Degradation rate (%)
Irradiation time (min)
0
10
20
30
40
50
60
70
0
30
60
90
120
150
180

Fig. 10

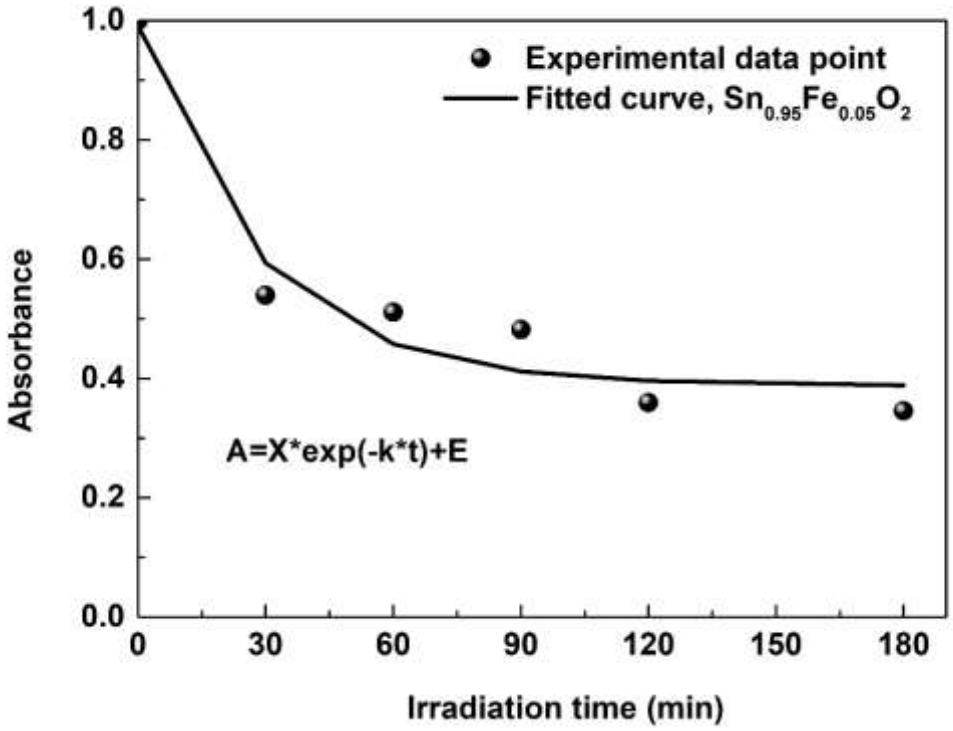
Experimental data point
Fitted curve, $Sn_{0.95}Fe_{0.05}O_2$
A=X*exp(-k*t)+E
Absorbance
Irradiation time (min)
1.0
0.8
0.6
0.4
0.2
0.0
0
30
60
90
120
150
180

Fig. 11

Figures

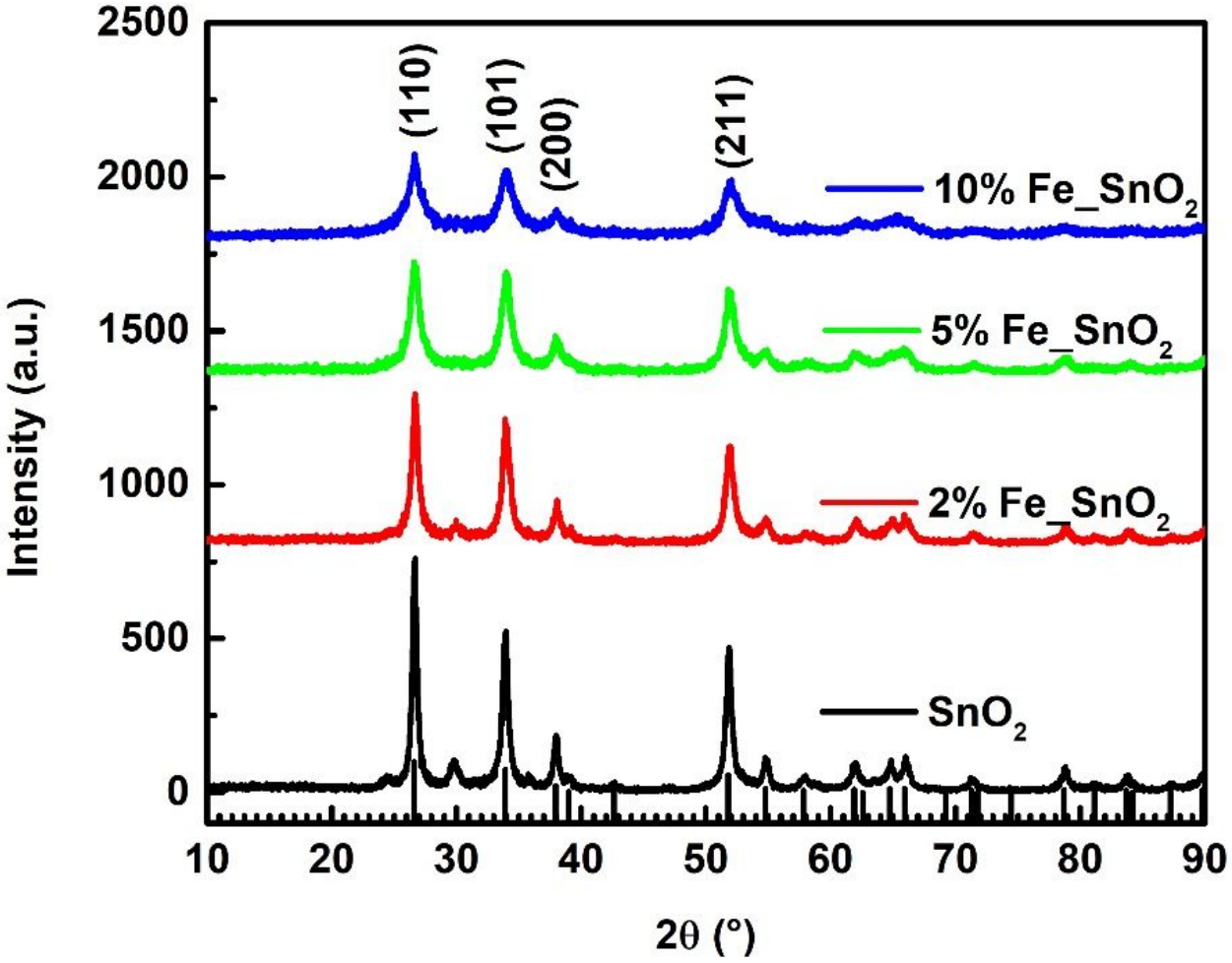

Figure 1

XRD patterns of SnO2 and Sn 1−xFexO2 (with x = 2, 5 and 10 at%) nanoparticles

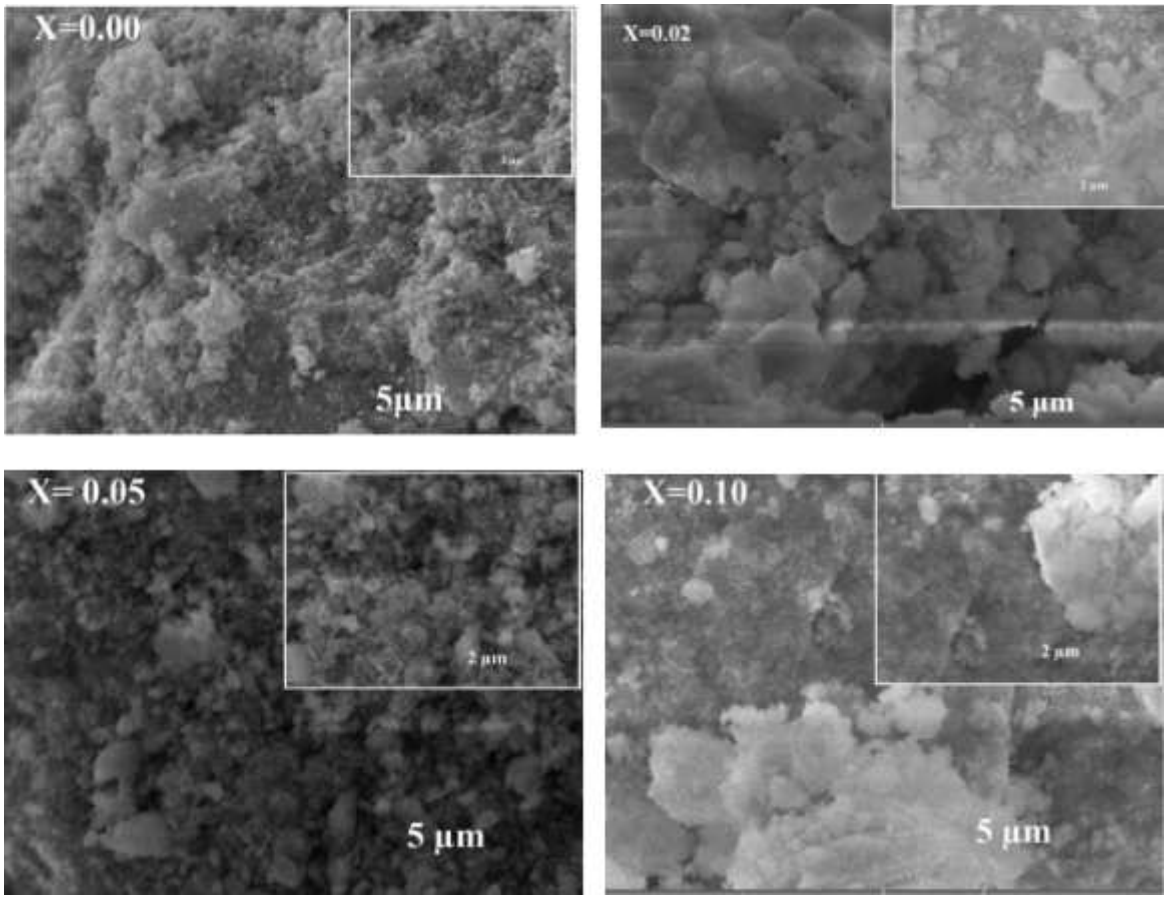

Figure 2

SEM images of Sn1-xFeXO2 [x=0, 2, 5 and 10 at%] nanoparticles.

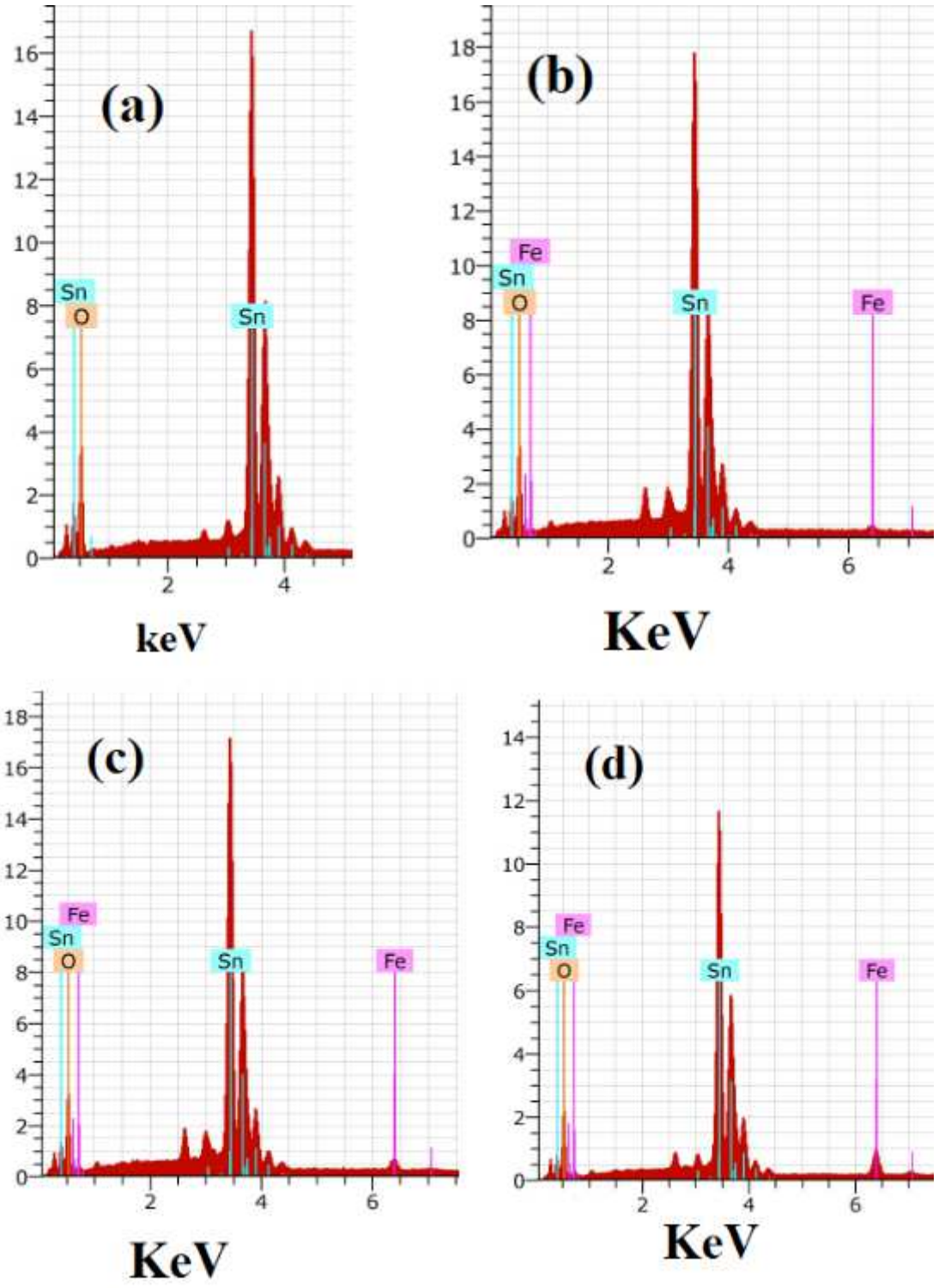

Figure 3

EDX elemental composition analysis of a pure SnO2 nanoparticles and b–d Fe–doped Sn1-xFeXO2 [x= 2,5 and 10] nanoarticles.

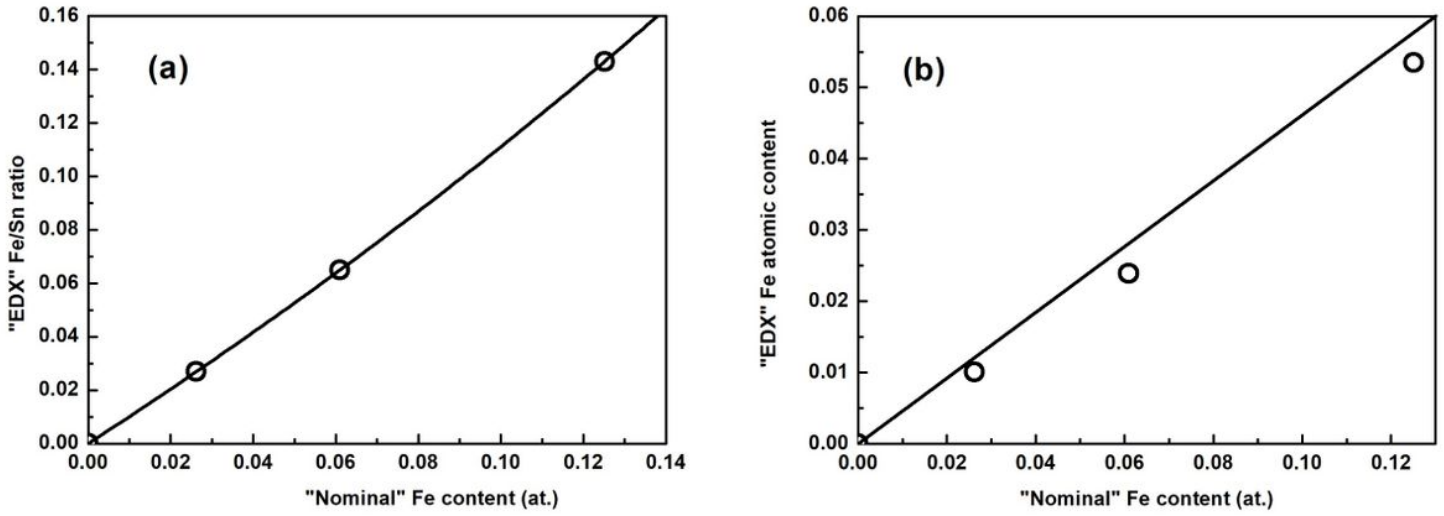

Figure 4

a The measured Fe/Sn atomic ratio and b the calculated Fe atomic content (from EDS analysis) plotted as function of the expected Fe content/doping

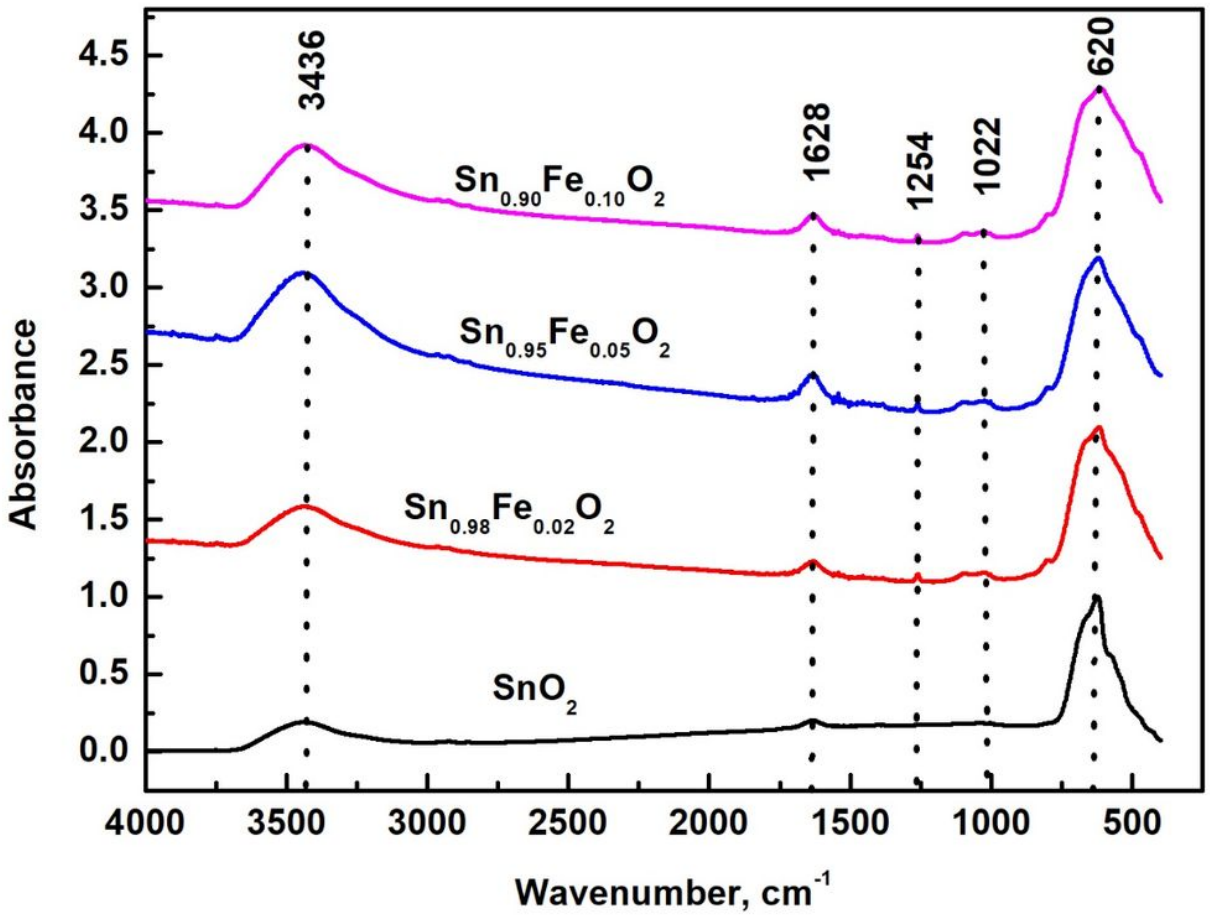

Figure 5

FTIR spectra of Sn1-xFeXO2 [x=0, 2, 5 and 10 at%] nanoparticles at room temperature in the wave number from 400 to 4000 cm-1

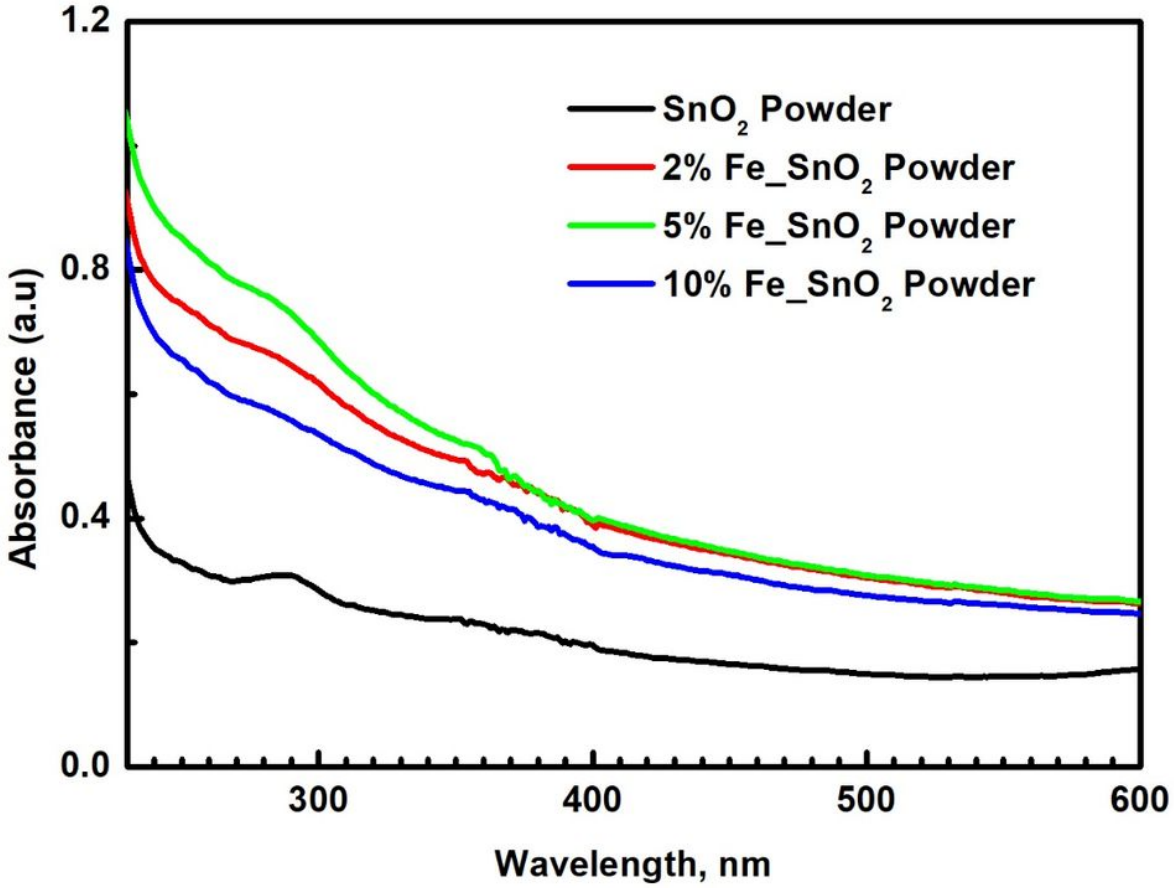

Figure 6

UV–Visible absorption spectra of Sn1-xFeXO2 [x=0, 2, 5 and 10 at%] nanoparticles.

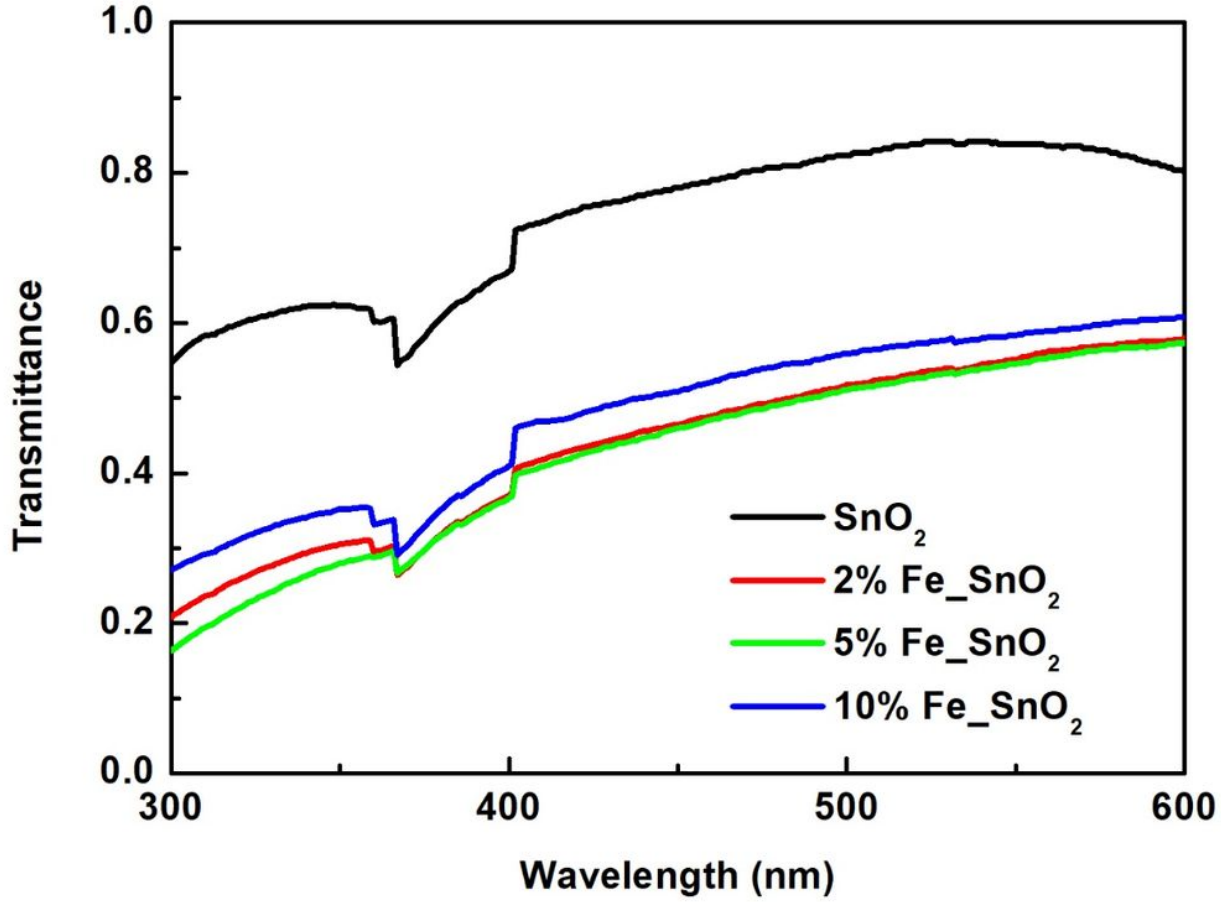

Figure 7

Transmittance spectra of of Sn1-xFeXO2 [x=0, 2, 5 and 10 at%] nanoparticles.

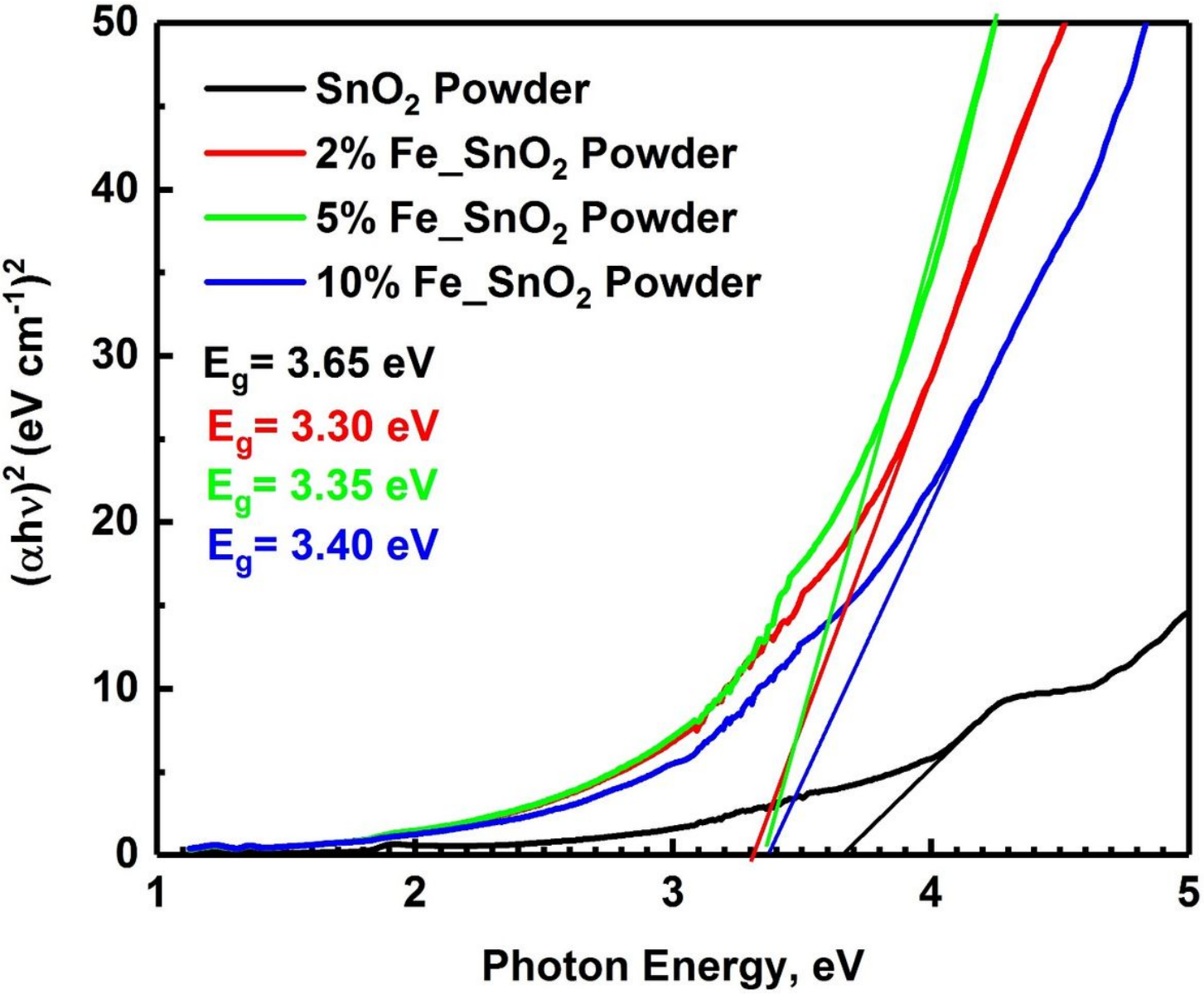

Figure 8

The (αhv)2 versus hv curves of of Sn1-xFeXO2 [x=0, 2, 5 and 10 at%] nanoparticles, for the optical energy gap calculation.

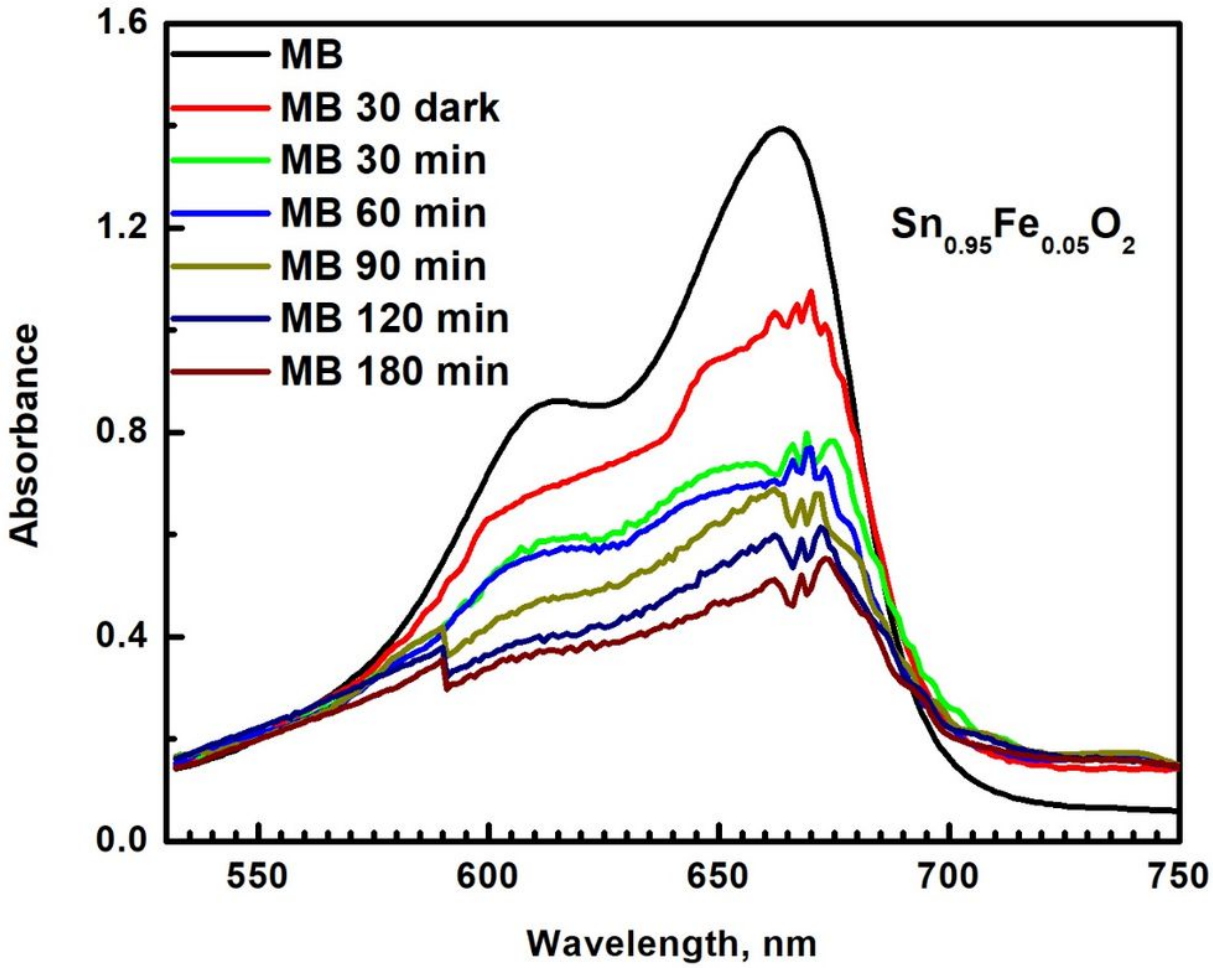

Figure 9

The effect of Sn0.95Fe0.05O2 nanoparticles on the absorption spectra of MB solution for different reaction time under UV irradiation.

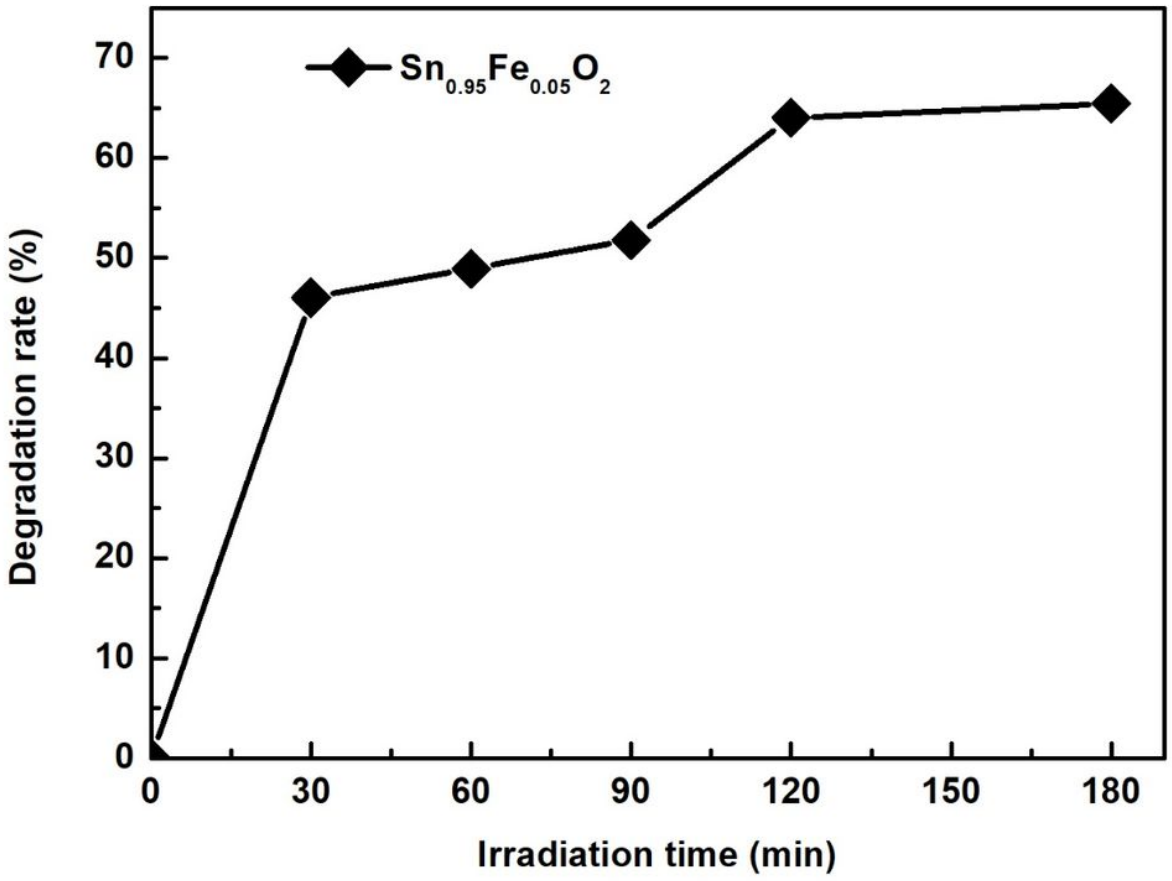

Figure 10

Degradation rate of Sn0.95Fe0.05O2 nanoparticles in MB degradation

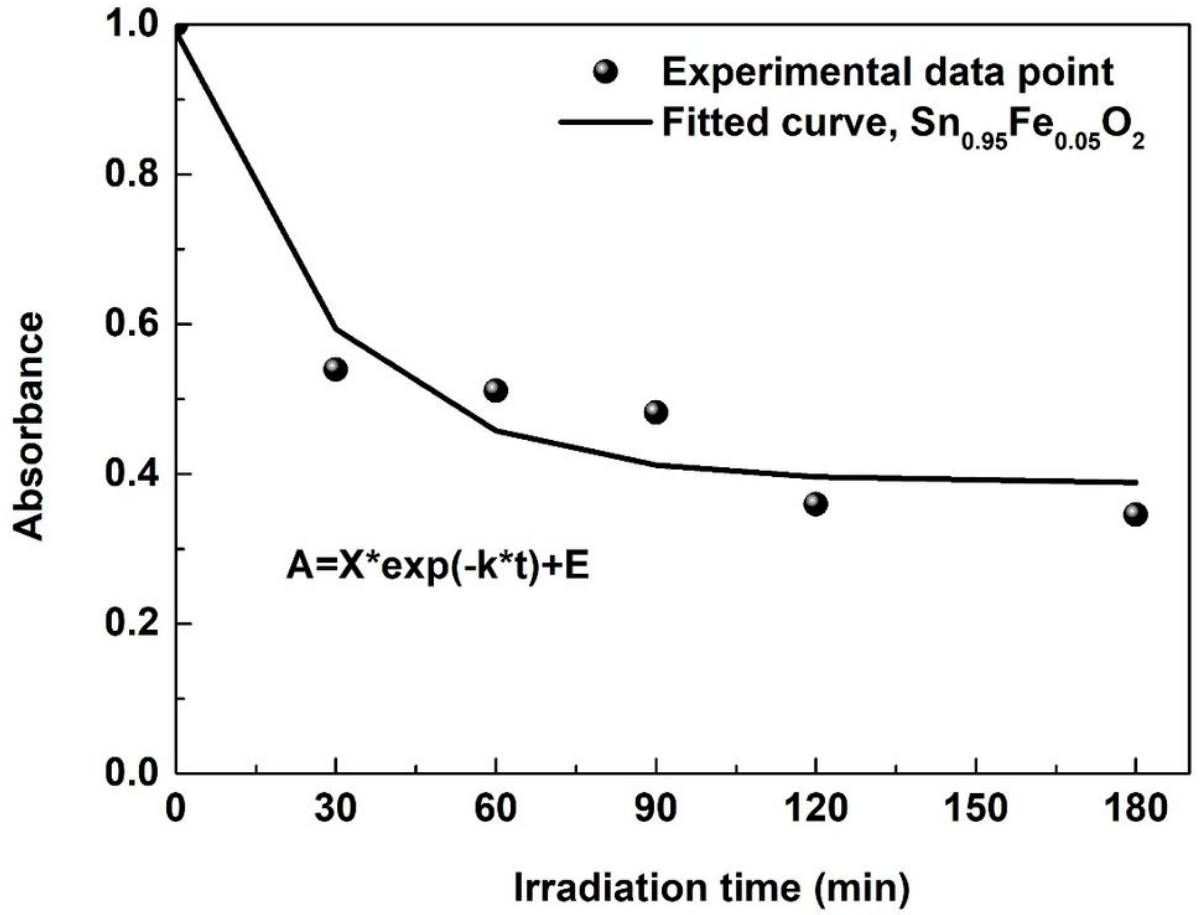

Figure 11

Decolorization kinetics of MB aqueous solutions by Sn0.95Fe0.05O2 nanoparticles without UV irradiation. The nanoparticles were prepared by using co-precipitation method. The photocatalytic process at UV-irradiation follows first-order kinetics according to the equation A=X*exp(-k*t)+E (cercles) Experimental data point and (solid lines) fitted curve (solid lines). Here A0 is the initial absorbance of the dye solution, A(t) is the absorbance at time t, and k is the rate constant of photocatalysis.